Are Supercells Resistant to Entrainment because of Their Rotation?

JOHN M. PETERS

Department of Meteorology, Naval Postgraduate School, Monterey, California

CHRISTOPHER J. NOWOTARSKI

Department of Atmospheric Sciences, Texas A&M University, College Station, Texas

GRETCHEN L. MULLENDORE

Department of Atmospheric Sciences, University of North Dakota, Grand Forks, North Dakota

(Manuscript received 12 November 2019, in final form 19 December 2019)

ABSTRACT

This research investigates a hypothesis posed by previous authors, which argues that the helical nature of the flow in supercell updrafts makes them more resistant to entrainment than nonsupercellular updrafts because of the suppressed turbulence in purely helical flows. It was further supposed that this entrainment resistance contributes to the steadiness and longevity of supercell updrafts. A series of idealized large-eddy simulations were run to address this idea, wherein the deep-layer shear and hodograph shape were varied, resulting in supercells in the strongly sheared runs, nonsupercells in the weakly sheared runs, and variations in the percentage of streamwise vorticity in updrafts among runs. Fourier energy spectrum analyses show well-developed inertial subranges in all simulations, which suggests that the percentages of streamwise and crosswise vorticity have little effect on turbulence in convective environments. Additional analyses find little evidence of updraft-scale centrifugally stable flow within updrafts, which has also been hypothesized to limit horizontal mass flux across supercell updrafts. Results suggest that supercells do have smaller fractional entrainment rates than nonsupercells, but these differences are consistent with theoretical dependencies of entrainment on updraft width, and with supercells being wider than nonsupercells. Thus, while supercells do experience reduced fractional entrainment rates and entrainment-driven dilution, this advantage is primarily attributable to increased supercell updraft width relative to ordinary convection, and has little to do with updraft helicity and rotation.

1. Introduction

Several aspects of supercell thunderstorms make them unique among other modes of deep convection. Supercell updrafts are capable of retaining a quasi-steady-state, plume-like updraft for upward of an hour (e.g., Doswell and Burgess 1993). Nonsupercellular convective updrafts, on the other hand, are typically composed of series of comparatively transient rising thermals (e.g., Bryan and Fritsch 2002; Sherwood et al. 2013; Romps and Charn 2015; Lebo and Morrison 2015; Hernandez-Deckers and Sherwood 2016). Though some nonsupercellular modes of deep convection (such as mesoscale convective systems) may last for more than an hour, the lifetimes of the individual thermals is often less than 15 min (e.g., Hernandez-Deckers and Sherwood 2016). Supercell updrafts tend to be relatively wide, sometimes exceeding 10 km in diameter (e.g., Peters et al. 2019b, hereafter P19). The diameter of thermals in ordinary convection, on the other hand, is often closer to 1 km or less (e.g., Sherwood et al. 2013; Hernandez-Deckers and Sherwood 2016). Supercells are capable of sending nearly pure boundary layer air well into the lower stratosphere, and consequently have core buoyancy that is very close to that of an undiluted air parcel lifted moist adiabatically (P19). Updraft cores in ordinary deep convection, on the other hand, are often substantially diluted (e.g., Romps and Kuang 2010a) by entrainment of midlevel environmental air. Supercells will therefore have larger updraft core buoyancy than ordinary convection if both share the same thermodynamic environment (e.g., P19). Supercells also exhibit

Corresponding author: J. Peters, jmpeters@nps.edu

DOI: 10.1175/JAS-D-19-0316.1

storm motions that are markedly different from the mean winds in the cloud-bearing layer, which is a consequence of continuous updraft propagation (e.g., Rotunno and Klemp 1982, 1985; Weisman and Rotunno 2000), and often results in stronger low-level storm-relative winds and inflow (P19). The low-level dynamic accelerations that are responsible for continuous updraft propagation continuously supply boundary layer air to its LFC, and thereby play an important role in supercell updraft persistence. These unique properties of supercells contribute to the largest vertical velocities among observed modes of atmospheric convection (Lehmiller et al. 2001; DiGangi et al. 2016), with the potential exception of volcanic eruptions and vigorous pyrocumulus (e.g., Peterson et al. 2018).

The intensity of supercell updrafts has often been attributed to updraft rotation. The rotational flow characteristic of supercell updrafts contributes to the separation of supercell updrafts and downdrafts (Klemp et al. 1981). Upward dynamic pressure accelerations below rotationally driven perturbation pressure minima drive continuous updraft propagation and therefore modulate storm motion (e.g., Rotunno and Klemp 1982, 1985; Weisman and Rotunno 2000). Upward rotationally driven dynamic pressure accelerations also substantially enhance vertical velocities in supercells' lower updrafts (e.g., Weisman and Klemp 1984; McCaul and Weisman 1996; Weisman and Rotunno 2000), which may contribute to larger overall updraft velocities and storm longevity. Finally, the stretching of near-surface vertical vorticity within supercell outflow is essential to the development of tornadoes (e.g., Davies-Jones et al. 2001).

It was hypothesized by Lilly (1986, hereafter L86) and Brandes et al. (1988, hereafter B88) that the helical nature of flow within supercell updrafts suppresses small-scale turbulence relative to nonhelical updrafts, owing to the nonisotropic nature of turbulence in helical flows (e.g., André and Lesieur 1977) (we will call this the "helicity hypothesis"). It was further supposed by L86 that the reduced turbulence in helical supercells makes the updrafts less susceptible to the deleterious effects of entrainment. Indeed, the entrainment of dry environmental air from the free troposphere strongly modulates updraft buoyancy (Romps and Kuang 2010b), such that reduced entrainment in supercells would make vertical accelerations in supercell updrafts stronger. Furthermore, Morrison (2017) showed that entrainment is responsible for the breakdown of updrafts into discrete transient thermals in ordinary convection, and reduced entrainment in supercells relative to ordinary convection may therefore make updrafts more persistent and stable. The helicity hypothesis was not rigorously tested by L86; rather, L86 referenced previous fluid studies that showed a reduction in small-scale energy in helical flows relative to nonhelical flows. He speculated that the reduction in small-scale turbulence may equate to reduced updraft entrainment and prolonged updraft stability in supercells. The hypothesis posed in B88, on the other hand, only pertained to a reduction in turbulence and did not explicitly mention the subsequent effects of turbulence on entrainment. Nonetheless, B88 did not examine the turbulence characteristics of supercell updrafts either, and the connection between helical flow in supercell updrafts and entrainment remains purely speculative. Of course, rigorous tests of either of these hypotheses were nearly impossible at the time, since simulations of deep convection only begin to develop a realistic inertial subrange of turbulence when the horizontal grid spacing is less than 250 m (e.g., Lebo and Morrison 2015), and computational resources largely precluded the use of grid spacing less than 1 km in the 1980s.

Vortices need not be helical (i.e., contain streamwise vorticity) for turbulence to be suppressed. Indeed, the toroidal circulations of dry and moist thermals are examples of vortices containing predominantly crosswise vorticity; however, these vortices also coincide with low dynamic pressure, and centrifugal stability causes a reduction in mixing between the interior and exterior of the vortex. Examples of this behavior are evident in a study of dry thermals by Tarshish et al. (2018, Figs. 3e–h in that study), wherein the centers of thermals' toroidal circulations retain local maxima in buoyancy relative to their surroundings because of reduced mixing between the interior of the toroidal circulations and the ambient environment. It is possible that supercell updrafts are centrifugally stable in an analogous manner to toroidal circulations, which protects the interiors of supercell updrafts from entrainment (we will call this the "centrifugal stability hypothesis").

Several characteristics of supercells noted by past literature, however, cast doubt on the idea that supercells are resistant to entrainment because of their rotation. The arguments in L86 and B88 were based on a theoretical analysis of Beltrami flow (i.e., flow characterized by purely streamwise vorticity); however, most supercell environments also contain substantial crosswise vorticity, which modifies updraft evolution from this ideal state (Weisman and Rotunno 2000). Furthermore, air parcels within supercells with predominantly cyclonic vorticity sometimes ascend along paths that curve in an anticyclonic manner (e.g., Klemp et al. 1981; Dahl 2017), which suggests that the motion of air parcels in supercells is quite different from that of cyclonic cyclostrophically balanced vortex. In fact, cross sections through

low-level supercell updrafts often exhibit an "open vortex," with flow resembling a rotating vortex only residing within the eastern flank of the updraft[1] (Dahl 2017).

Updraft width is another attribute of supercells that dictates entrainment properties. Both Warren et al. (2017) and Trapp et al. (2017) noted that supercell updraft width and the vertical wind shear magnitude tend to be correlated. Our recent work in P19 used both simulations and theory to show that supercell updrafts tend to be much wider than nonsupercellular updrafts because larger vertical wind shear promotes faster storm motion and consequently increases low-level, storm-relative flow in the environments of supercells. By comparing boundary layer tracer concentrations and updraft buoyancy among simulations with different deep-layer wind shear magnitudes, we further showed in P19 that supercell updrafts in strong shear experienced less core dilution of buoyancy than nonsupercell updrafts in comparatively weaker shear. Indeed, theory suggests that fractional entrainment rates are inversely proportional to updraft width (e.g., Lecoanet and Jeevanjee 2019), meaning that wider updrafts will entrain less per unit vertical mass flux at a given height than narrower updrafts. Furthermore, Morrison (2017) showed that because wider updrafts have smaller fractional entrainment rates, they are less susceptible to breaking down into discrete transient thermals than their narrower counterparts. These arguments suggest that supercells may be resistant to the deleterious effects of lateral entrainment because they are wider than ordinary updrafts (we will call this the "width hypothesis").

The central purpose of this study is to isolate the potential influences of updraft rotation and width on entrainment in supercells in order to test the three hypotheses described above. Note that the effects of updraft width and rotation on entrainment are not mutually exclusive. In fact, it is possible that supercells experience a reduction in entrainment due to both rotation and width. It is also important to note that other factors beyond entrainment, such as dynamic pressure perturbation accelerations or downshear precipitation displacement, may prolong or intensify supercell updrafts. Though a few of the studies cited in this section have also referenced connections between rotation and updraft longevity, we emphasize that the focus of our analysis is restricted to the connections between rotation and entrainment. The organization of this paper is as follows: section 2 gives an overview of the numerical simulations that were used to address these three hypotheses, section 3 describes our methods for quantitatively analyzing simulations, section 4 details the results from our quantitative analysis, and section 5 provides a summary, conclusions, and discussion.

[1] Note that this discussion neglects the formation of consolidated tornado-like vortices, which are centrifugally stable. Such tornado-like vortices are only present during a small percentage of the lifetime of some supercells and therefore cannot explain the overall intensity of supercell updrafts.

2. Numerical simulation methods

a. Overview

We ran a series of large-eddy simulations to evaluate the hypotheses discussed in section 1, wherein the shape and shear magnitude of the environment wind profile were varied among simulations. Some of these simulations produced transient nonsupercellular convection and some produced sustained supercells. To address the helicity hypothesis, we first determined whether the flow within our simulated supercell updrafts is helical, and then assessed whether variations in helical nature of updrafts corresponded to differences in turbulence and entrainment. To address with width hypothesis, we looked for a strong dependence of entrainment on updraft width. Finally, to address the centrifugal stability hypothesis, we looked for large regions of centrifugally stable flow within supercell updrafts and accordingly reduced turbulence in these areas relative to nonsupercellular updrafts.

b. Model configuration

All simulations were run using Cloud Model 1 (CM1; Bryan and Fritsch 2002), version 18, which is a nonhydrostatic, semicompressible numerical model that features an acoustic time-splitting dynamical core. CM1 is designed for simulating clouds (as the name suggests) within a background environment characterized by a single initial sounding. Domain dimensions were 100.8, 100.8, and 22 km in the x, y, and z directions, respectively (the extra 0.8 km in the x and y directions was included to satisfy the multithreading requirements of the model). Horizontal and vertical grid spacing was isotropic at 100 m, and a nonacoustic time step of 0.9 s was necessary to ensure numerical stability. Radiation and surface physics were turned off, and free-slip bottom and top boundary conditions were used. Microphysical processes were parameterized using the Morrison et al. (2009) double-moment scheme. Lateral boundary conditions were "open radiative" using the method of Durran and Klemp (1983). To facilitate the development of realistic turbulence, all simulations were initialized with random temperature perturbations drawn from a uniform distribution with maximum amplitudes of 0.25 K. Simulations were run for

TABLE 1. Summary of the CM1 configuration.

Attribute	Value/setting	Notes
Time-splitting vertically implicit pressure solver	Yes	
Horizontal grid spacing	100 m	
Vertical grid spacing	100 m	
Nonacoustic time step	0.9 s	
Vertical coordinate	Height (m)	
Number of x and y points	1008×1008	
Vertical points	220	
Top and bottom boundary conditions	Free slip	
North and south lateral boundary conditions	Open radiative	Durran and Klemp (1983)
East and west lateral boundary conditions	Open radiative	Durran and Klemp (1983)
Convection initiation	Warm bubble at domain center, horizontal radius: 5 km, vertical radius: 1.4 km, θ perturbation: 3 K	
Microphysics	Morrison	Morrison et al. (2009)
Advection	Fifth order	
Subgrid turbulence	TKE	
Rayleigh dampening	Yes	
Dissipative heating	Yes	
Second- and sixth-order diffusion coefficient	75–0.04	
Longwave radiation	—	
Shortwave radiation	—	
Surface layer	—	
Boundary layer physics	—	
Cumulus parameterization	—	

3 h with model data output every 5 min. Domain translation speeds were set to approximately center storms within the domain. Because both entrainment and centrifugal stability computations (see below) require high temporal resolution, we restarted a 10-min period in each simulation and output data at 5-s intervals during this period. Limited disk storage and computational resources prohibited longer periods with 5-s output, but examinations of different time periods than the ones extensively analyzed here offer qualitatively similar results that affirm our conclusions. The bulk of subsequent analysis will focus on these high-temporal-frequency output time periods, and the timing of this period for each simulation is outlined at the beginning of section 4. A summary of the modeling configuration is provided in Table 1.

The initial model thermodynamic profiles use modified versions of the analytic sounding from Weisman and Klemp (1982, hereafter the WK82 sounding) (Fig. 1a). The relative humidity was set to 45% above 3 km because previous authors have noted that the WK82 sounding, in its original formulation, is unrealistically moist in the middle to upper troposphere (e.g., Potvin and Flora 2015). To add thermodynamic variability to our simulations, we used two different boundary layer moisture values of 14 and 16 g kg^{-1}, yielding two different convective available potential energy (CAPE) values and mixed-layer depths (0–1-km mean CAPE values of 1729 and 2744 J kg^{-1}, respectively). Runs with 14 and 16 g kg^{-1} are referred to as LOWCAPE and HICAPE, respectively.

Initial model wind profiles were designed to elucidate the potential connections between updraft rotation, width, and entrainment. Wind profiles were either half-circle shaped (hereafter "CIR") or straight shaped (hereafter "STR") (Fig. 1b). When half-circle- and straight-shaped wind profiles have similar bulk wind shear and storm-relative flow magnitudes, half-circle-shaped profiles tend to have much larger low-level storm-relative helicity (SRH). For instance, the SRH in the CIR HISHR simulations can be over twice as large as SRH in the STR HISHR simulations (Fig. 2a), whereas differences in bulk wind difference (Fig. 2b) and mean storm-relative (SR) flow are only ~10%–20%. We will use these low-level SRH differences among simulations, and the influence of these SRH differences on the percentage of vorticity that is streamwise in the updraft, to determine whether certain hodograph shapes afford storms more reduced turbulence and entrainment than others. The wind above 6 km was held constant in all simulations.

Three different shear configurations, which are termed "LOW," "MED," and "HI," were used for each profile

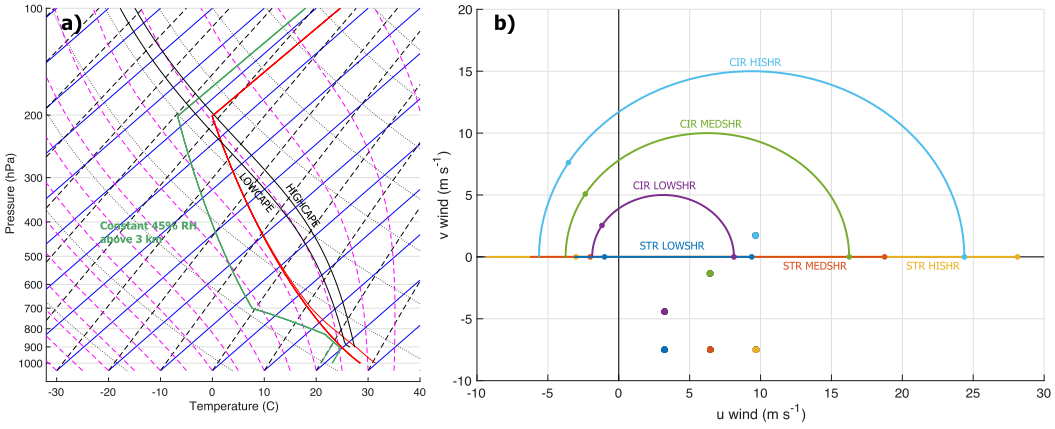

FIG. 1. (a) Skew T–log$p$ diagram showing the initial model profiles of temperature (thick red line), virtual temperature (thin red line), dewpoint temperature (green lines), and the virtual temperature of air parcels with the average properties of the lowest 1 km of the atmosphere, lifted moist adiabatically (black lines, with LOWCAPE corresponding to the left black line and HICAPE corresponding to the right black line). Note that the different boundary layer mixing ratio values in the LOWCAPE and HICAPE runs (see the two green lines at the bottom of the figure) yielded two different lifted parcel profiles. (b) Hodographs corresponding to the CIR LOWSHR (purple), CIR MEDSHR (green), CIR HISHR (light blue), STR LOWSHR (dark blue), STR MEDSHR (red), and STR HISHR (orange) profiles. Dots along hodograph curves indicate the 1- and 6-km winds, respectively. Dots separate from the curves are right-moving storm-motion vector estimates based on the Bunkers ID method (e.g., Bunkers et al. 2000).

shape to drive variation in updraft morphology and width. As will be shown later, the LOW runs produced narrow multicellular clusters with a distinctly thermal-like character to updrafts. In contrast, the MED runs produced wider plume-like updrafts with some supercellular characteristics, and the HI runs unambiguously produced wide plume-like supercell updrafts. These variations in updraft morphology and width facilitated the comparison between entrainment and turbulence in supercells and nonsupercells. Note that it is impossible to match shear through all layers between the CIR and STR profiles. For instance, 0–1- and 0–3-km shear values were larger in the CIR profile for a given shear configuration (e.g., for both the CIR and STR MID shear runs), whereas 0–6-km shear vales were larger in the STR profiles (Fig. 2b). Conversely, the STR profiles had larger 0–1-km mean SR flow but weaker 0–3-km mean SR flow than the CIR profiles (Fig. 2c). However, these

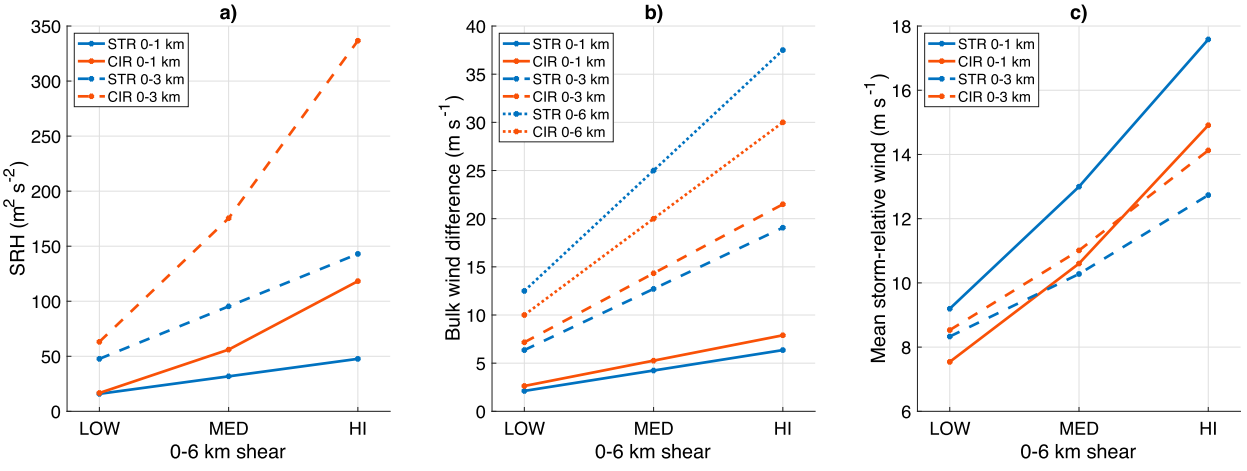

FIG. 2. Severe weather parameters for the initial model wind profiles as a function of the variations in 0–6-km shear among the runs. (a) 0–1- km (solid lines) and 0–3-km (dashed lines) storm-relative helicity (SRH) computed using the storm-motion estimates in Fig. 1. (b) 0–1-km (solid lines), 0–3-km (dashed lines), and 0–6-km (dotted lines) bulk wind differences. (c) 0–1- and 0–3-km mean storm-relative wind speeds computed using the storm-motion estimates in Fig. 1. In all panels, blue lines represent the STR profiles and red lines represent the CIR profiles.

differences do not affect our conclusions because we do not require shear to be held constant between the STR and CIR experiments. We name simulations based upon the combination of hodograph shape, shear magnitude, and the thermodynamic profile. For instance, a half-circle hodograph with the highest shear magnitude and smaller mixed-layer moisture/CAPE is referred to as the CIR HISHR LOWCAPE run.

3. Quantitative analysis methods

a. Defining updrafts

Because of widespread nonsupercellular convection in the runs that also contained sustained supercells, it was necessary to isolate supercell updrafts from nonsupercellular updrafts in order to make an effective comparison between these two modes of convection. To accomplish this, we first computed 1–4-km mean updraft helicity (UH = $w\zeta$, where w is vertical velocity and ζ is vertical vorticity). We then masked regions with either 1–4-km mean w less than 3 m s^{-1} and/or negative 1–4-km mean UH. We considered the primary "updraft of interest" to be the largest persistent right-moving storm within the domain, which was assumed to correspond with the largest unmasked continuous positive area of 1–4-km mean UH. The centroid of the updraft x_c and y_c was found by averaging the x and y points contained within this region. The three-dimensional extent of the supercell updraft was then defined as a continuous volume of grid points with $w > 10$ m s^{-1} containing the centroid point at an altitude of 3 km. Since entrainment rates are often related to updraft radius, we computed the effective updraft radius R_{eff} at a given height as $\sqrt{A/\pi}$, where A was the area of the updraft at a given height. This procedure was applied to all of the HISHR runs, which unambiguously produced supercells.

The aforementioned procedure was less effective at identifying nonsupercell updrafts due to their discontinuous, transient, and thermal-like nature. We therefore included all areas with $w > 10$ m s^{-1} that occurred within 10 km of the grid point of maximum domain w in all of the LOWSHR runs, the STR MEDSHR HICAPE run, and the CIR MEDSHR LOWCAPE run. An exception to this rule is for updraft width estimates. Since it is possible for multiple updrafts to be present on a given level in this situation, we used the largest continuous area with $w > 10$ m s^{-1} on a given vertical level to compute nonsupercell updraft R_{eff}.

In later computations, it was necessary to compute the storm-relative wind field using the motion of simulated updrafts. In all the simulations where a primary supercellular updraft was tracked and identified (e.g., the HISHR, STR MEDSHR LOWCAPE, and CIR MEDSHR HICAPE runs), updraft motion was computed as the velocity of the updraft centroid ($c_x = dx_c/dt$, $c_y = dy_c/dt$), with a Gaussian smoothing filter with radius of influence of 1 min applied. In the STR MEDSHR HICAPE simulation, wherein the high-frequency output period began at 180 min, the storm motion was estimated as $c_x = 3$ m s^{-1} and $c_y = -3.3$ m s^{-1} based on the change in position of the storm between 120 and 180 min. In the CIR MEDSHR runs and all of the LOWSHR runs, the domain-relative updraft motion was very small during the high-temporal-frequency output period at 10 min, so the speed of the updraft relative to the domain was set to 0 m s^{-1}.

b. Quantifying turbulence

Fourier energy spectrum (FES) analysis is often used to evaluate the turbulence characteristics of fluids (e.g., Bryan et al. 2003; Lebo and Morrison 2015; Peters et al. 2019a). FES shows the distribution of kinetic energy within a fluid as a function of scale. To compute the FES, we first take the one-dimensional discrete Fourier transform of w at a given level in both the x and y directions to obtain $U_x(k)$ and $U_y(k)$, respectively, where k is a horizontal wave number. The two-dimensional energy spectra are defined as $E(k) = 2\pi[U_x^2(k) + U_y^2(k)]$. To evaluate $E(k)$ for each discrete k, we averaged $2\pi[U_x^2(k) + U_y^2(k)]$ over the range $k - \Delta k$ through $k + \Delta k$, where $\Delta k = (2\pi/100)$ m^{-1}.

For fully turbulent flow, we expect E to decrease monotonically for κ larger than the wavenumber with peak energy, with a slope that eventually approaches $\kappa^{-5/3}$ in accordance with Kolmogorov's law. In numerical simulations with finite grid spacing, κ often follows a $-5/3$ slope through a small fraction of large wavenumbers before trailing off at a steeper slope near the effective grid resolution of the model, which is often quoted at 5 to 6 times Δx (Bryan et al. 2003; Lebo and Morrison 2015). This region of the energy spectrum that follows a $-5/3$ slope is often referred to as the "inertial subrange." Any potential influence of the presence or absence of streamwise vorticity on turbulence within flow will therefore be evident in the appearance of or absence of an inertial subrange within FES analysis of model data.

c. Quantifying entrainment

A common definition for entrainment in the literature is the rate at which air parcels that are not part of an updraft become part of the updraft (e.g., Romps 2010; Dawe and Austin 2011). This concept can be understood mathematically by defining a quantity σ that is set to 1 if air parcels meet a criteria for being part of an updraft (e.g., $w > 3$ m s^{-1}), and set to 0 elsewhere. Based on this

definition, the total entrainment at a given height is (e.g., Romps 2010)

$$\epsilon(z,t) \equiv \iint \max\left[\frac{D}{Dt}(\rho\sigma), 0\right] dA, \tag{1}$$

wherein the horizontal integral is evaluated over an entire analysis domain at a given height. Note $\epsilon(z, t)$ is not restricted to merely lateral entrainment. For instance, this quantity will register an upward or downward flux of mass through a vertically oriented cloud surface as an "entrainment event," as well as lateral fluxes across lateral cloud surfaces. Furthermore, previous authors have often distinguished between "dynamic entrainment," which occurs with the cloud's organized inflow and outflow structures, from "turbulent entrainment," which is accomplished by mixing that occurs on scales that are much smaller than that of the cloud as a whole (e.g., De Rooy and Siebesma 2010). Both of these types of entrainment are thought to play important roles in influencing cloud properties, and both are measured by the direct calculation for entrainment that we are using here.

The total entrainment ϵ should actually increase as updraft width increases. Consider the simple example of a steady-state axisymmetric cylindrical updraft with constant radius R where the speed of entrained air s is constant. In this case, the entrainment at a given updraft level is simply the horizontal flux of mass across the updraft boundary $\epsilon = 2\pi sR\rho$ ($\mathrm{kg\,s^{-1}\,m^{-1}}$). It is clear from this expression that larger updrafts entrain more air than smaller updrafts, which seems to contradict statements made in the introduction. However, the primary influence of entrainment on updrafts is to dilute updraft core properties such as buoyancy, such that the updraft core dilution is more relevant than the total entrainment. If we divide ϵ by the vertical mass flux $M = \pi\overline{w}\rho R^2$, we obtain the fractional entrainment $\varepsilon \equiv \epsilon/M = 2s/R\overline{w}$ (where $\overline{w}$ is the updraft-averaged w on a given level). Fractional entrainment ε gives a better estimation for the rate at which an updraft core is diluted, and we see that as updrafts become wider and faster, ε tends to decrease because an updraft's cross-sectional area increases faster with R than its perimeter area.

Returning to the quantitative definition of ϵ in Eq. (1), we obtained ε from ϵ using

$$\varepsilon(z,t) \equiv \frac{\epsilon}{\iint \rho w\sigma\, dA}, \tag{2}$$

where $\iint \rho w\sigma\, dA$ is the updraft mass flux at a given level. The computation of Eq. (1) was performed on a gridpoint-by-gridpoint basis by expanding the Lagrangian derivative into its Eulerian components. Note that this computation requires special numerical considerations since this expression contains advective terms. Details of these considerations are explained thoroughly in the appendices of Romps (2010).

d. Diagnosing helicity

The degree to which flow is helical is directly measured via the quantity relative helicity H_{rel}, which is defined as

$$H_{\mathrm{rel}} \equiv \frac{\mathbf{V}\cdot\boldsymbol{\omega}}{|\boldsymbol{\omega}||\mathbf{V}|}, \tag{3}$$

where $\mathbf{V}$ is the three-dimensional wind vector and $\boldsymbol{\omega} = \nabla \times \mathbf{V}$ is the vorticity vector. Note that streamwise vorticity is defined as $\boldsymbol{\omega}_s \equiv (\mathbf{V}/|\mathbf{V}|)\cdot\boldsymbol{\omega}$, so $H_{\mathrm{rel}} = \boldsymbol{\omega}_s/|\boldsymbol{\omega}|$ is also a measure of the fraction of vorticity that is streamwise. For helical flow, wherein vorticity is predominantly streamwise, $H_{\mathrm{rel}} \to 1$, whereas for flow characterized by purely crosswise vorticity, $H_{\mathrm{rel}} \to 0$. Note that H_{rel} is not Galilean invariant, since $\mathbf{V}$ depends on the frame of reference. It is therefore common practice to compute H_{rel} with the storm-relative wind field. We therefore concentrated our analysis on the frame of reference moving with the primary supercell thunderstorm of interest in the simulations by subtracting the storm-motion vector $\mathbf{C}$ from the ground-relative wind field in order to compute H_{rel}.

To understand the role of helical flow in reducing turbulence and entrainment in supercells, L86 drew analogies between flow within supercell updrafts and theoretical Beltrami flow. In Beltrami flow, the vorticity vector $\boldsymbol{\omega}$ points in the same direction as $\mathbf{V}$ such that $\boldsymbol{\omega} = k\mathbf{V}$, where k is a function of space and time. Beltrami flow shares many properties of potential flow, such as a quasi linearization of many of the equations of motion. For example, nonlinear advection, stretching, and tilting terms in the vorticity equation balance each other in Beltrami flow. Since processes related to these terms are essential to the downscale cascade that leads to an isotropic turbulence energy spectrum, turbulence is inhibited in Beltrami flow.

Now, Beltrami flow does not exist in natural convective updrafts, in part because horizontal buoyancy gradients on the updraft periphery readily generate crosswise vorticity (the formation of toroidal circulations are an example of this). Relative helicity in supercell updrafts, on the other hand, is often very high (>0.9 in the simulations performed by L86), indicating that vorticity is largely streamwise. What our analysis will clarify is whether flows with low (but nonzero) fractions of crosswise vorticity experience reductions

in turbulence relative to less helical flows, or if purely streamwise flows are required for *any* suppression of turbulence in supercell updrafts.

e. Diagnosing centrifugal stability

To obtain a diagnostic to evaluate the horizontal centrifugal stability of flow, we used the inviscid horizontal momentum equations in natural coordinates [e.g., Eqs. (3.9) and (3.10) in Holton (2004)]:

$$\frac{D_H V}{Dt} = -\alpha_0 \hat{\mathbf{t}} \cdot \nabla_H p, \tag{4}$$

and

$$\frac{V^2}{R} = -\alpha_0 \hat{\mathbf{n}} \cdot \nabla_H p, \tag{5}$$

where D_H/Dt is the horizontal material derivative, $V \equiv |\mathbf{V}_H|$, $\mathbf{V}_H$ is the horizontal *storm-relative* wind vector, ∇_H is the horizontal gradient operator, $\hat{\mathbf{t}} \equiv \mathbf{V}_H/V$ is a horizontal unit vector in the direction of the wind, R is the radius of curvature, and $\hat{\mathbf{n}}$ is a horizontal unit vector orthogonal to $\hat{\mathbf{t}}$ that points in the direction of decreasing pressure. For flow in local cyclostrophic balance, $\hat{\mathbf{n}}$ and $-\nabla_H p$ point in the same direction, such that $\hat{\mathbf{t}}$ is orthogonal to $\nabla_H p$ and $D_H V/Dt$ vanishes. In purely unbalanced flow (i.e., flow that is accelerating directly with the pressure gradient force), $\hat{\mathbf{t}}$ and $-\nabla_H p$ point in the same direction and the radius of curvature R vanishes. Thus, the angle $\phi = \cos^{-1}[-(\nabla_H p \cdot \hat{\mathbf{n}}/|\nabla_H p|)]$ between $\hat{\mathbf{n}}$ and $-\nabla_H p$ measures the degree to which air parcel motions are cyclostrophically balanced, with $\phi = 0$ implying an exact balance and $\phi = 90°$ implying no balance. In combining Eqs. (4) and (5), we obtain $D_H\hat{\mathbf{t}}/Dt = \hat{\mathbf{n}}V/R$, and solving for R and $\hat{\mathbf{n}}$ gives

$$R = \left| \frac{1}{V} \frac{D_H}{Dt} \left(\frac{\mathbf{V}_H}{V} \right) \right|^{-1} \tag{6}$$

and

$$\hat{\mathbf{n}} = \frac{R}{V} \frac{D_H}{Dt} \left(\frac{\mathbf{V}_H}{V} \right). \tag{7}$$

For the Eulerian calculations analyzed later, $D_H/Dt = \partial/\partial t + u(\partial/\partial x) + v(\partial/\partial y)$ of a given quantity was computed using second-order centered-in-space and centered-in-time finite difference approximations to the partial derivatives.

A condition for centrifugal stability in cylindrical coordinates $(d/dr)(\alpha_0 r^3 \partial p/\partial r) > 0$ was derived by Markowski and Richardson [2010, Eqs. (3.19)–(3.31) therein]. Such a condition is difficult to obtain for flow in natural coordinates where the central axis of rotation varies with time and space. However, a centrifugally balanced vortex requires spatially averaged flow over a broad region to exhibit cyclostrophic wind balance (though local perturbations associated with centrifugal waves may deviate from cyclostrophic balance). We therefore assume that the presence of broad regions of flow in cyclostrophic balance implies the presence of centrifugal stability, and search for regions within the updraft with $\phi \approx 0$, and take the presence of these regions to imply centrifugal stability.

4. Results

a. General characteristics of simulations

The LOWSHR simulations produced initial transient updrafts and radar reflectivity characteristics that marginally resembled supercell thunderstorms, including weakly defined hook echoes and the downshear transport of the bulk of precipitation to the north and northeast of the updraft region in (Figs. 3a,b and 4a,b). These initial convective features decayed within 90 min of the start of the simulations. In the HICAPE simulations, a squall line eventually developed along the eastern edge of the cold pool (not shown). Vertical cross sections through the updraft at 65 min (Figs. 5a,c,e) show updrafts to be composed of a series of semidiscrete rising thermals with updraft core widths in the vicinity of 1–3 km (this thermal-like behavior was prevalent among all LOWSHR simulations). This structure is consistent with numerous previous LES studies of nonsupercellular convection (e.g., Bryan and Fritsch 2002; Sherwood et al. 2013; Romps and Charn 2015; Lebo and Morrison 2015; Hernandez-Deckers and Sherwood 2016), and we therefore use these simulations as a nonsupercell "baseline" to which the characteristics of supercells will be compared. We selected the 60–70-min time period in each of these simulations for the high-temporal-frequency output period.

The MEDSHR convection behaved somewhat differently between the STR and CIR wind profiles. In the STR MEDSHR simulations, a north-to-south-oriented line of convection formed with a persistent supercell along the southern flank of the line (Figs. 3c and 4c). In the STR MEDSHR LOWCAPE simulation, this supercell maintained a structure akin to a classic supercell with a defined hook echo and "V notch" signature in the forward-flank precipitation through the end of the simulation (Fig. 3c). In the STR MEDSHR HICAPE simulation, on the other hand, the storm took on a more outflow-dominant appearance with substantial precipitation in the vicinity of the updraft and rapid

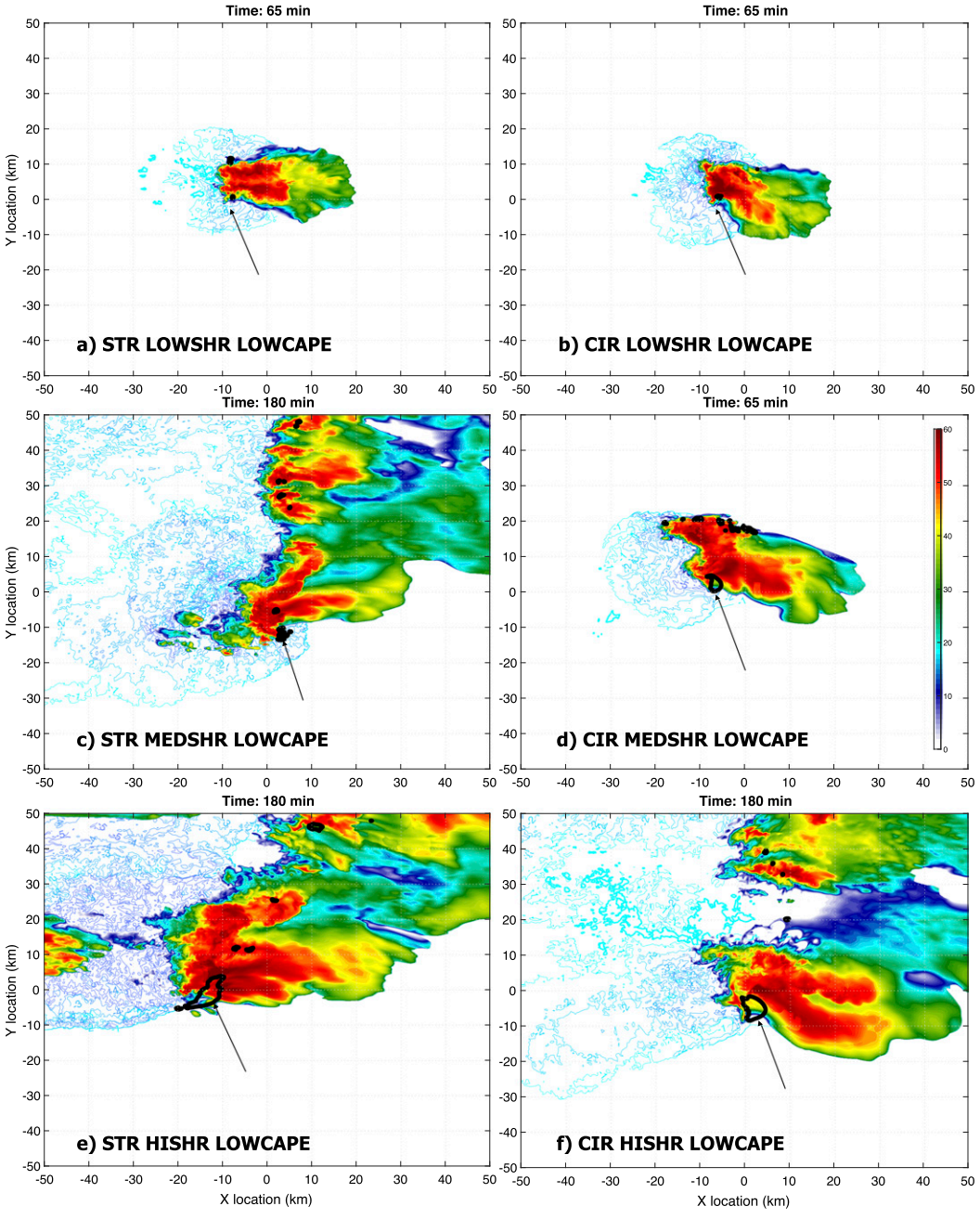

FIG. 3. Simulated radar reflectivity factor at 1 km (shading; dBZ), surface potential temperature differences from the initial model profile (blue contours starting at −1 K, and decreasing at intervals of −1 K), and the 6 m s^{-1} 1–4-km mean w contour (solid black line). (a) The STR LOWSHR LOWCAPE run at 65 min. (b) The CIR LOWSHR LOWCAPE run at 65 min. (c) The STR MEDSHR LOWCAPE run at 180 min. (d) The CIR MEDSHR LOWCAPE run at 65 min. (e) The STR HISHR LOWCAPE run at 180 min. (f) The CIR HISHR LOWCAPE run at 180 min. Arrows denote the location of the analyzed storm.

updraft occlusions and reformations (Fig. 4c). In contrast with the STR MEDSHR simulations, the CIR MEDSHR simulations both produced a transient supercellular feature that lasted roughly 2 h before dissipating (Figs. 3d and 4d). Vertical cross sections through all of the MEDSHR storms revealed a wider updraft than in the LOWSHR storms that was more akin to a continuous plume of rising air, rather than a succession of discrete rising thermals (e.g., Figs. 5b,d,f). The high-temporal-frequency output period was started at

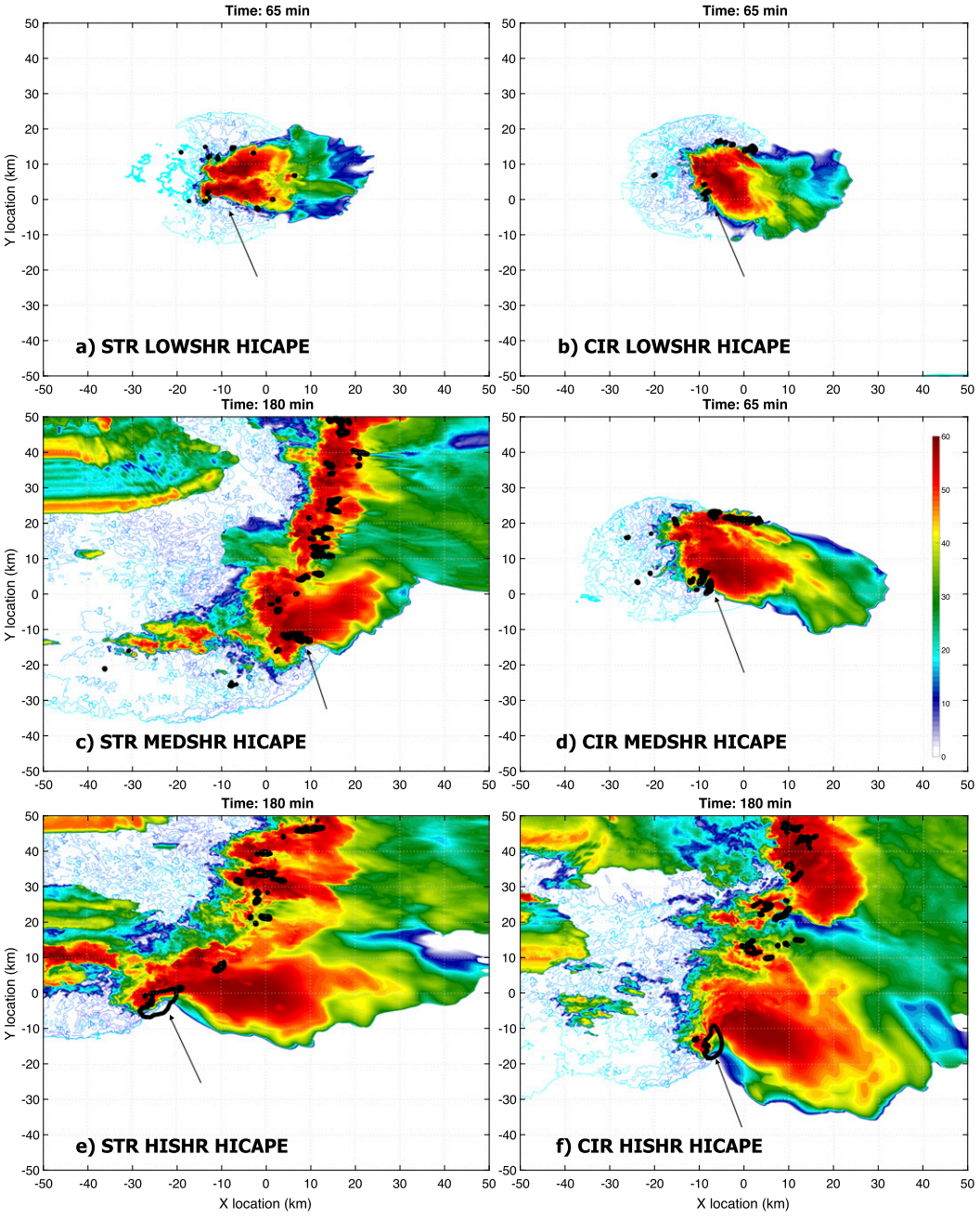

FIG. 4. As in Fig. 3, but for the HICAPE runs. (a) The STR LOWSHR HICAPE run at 65 min. (b) The CIR LOWSHR HICAPE run at 65 min. (c) The STR MEDSHR HICAPE run at 180 min. (d) The CIR MEDSHR HICAPE run at 65 min. (e) The STR HISHR HICAPE run at 180 min. (f) The CIR HISHR HICAPE run at 180 min.

180 min in the STR MEDSHR simulations because there was a persistent updraft from shortly after the simulation start through this time, whereas the high-temporal-frequency output period was started at 60 min in the CIR MEDSHR simulations due to the transient nature of the initial updrafts that formed in these simulations. Note that it is not necessary that the high-temporal-output time periods match up between simulations. Rather, our goal is to compare time periods from the lower shear simulations with a convective structure that is representative of nonsupercellular convection, to time periods from the higher shear simulations wherein the convective structure is representative of supercells.

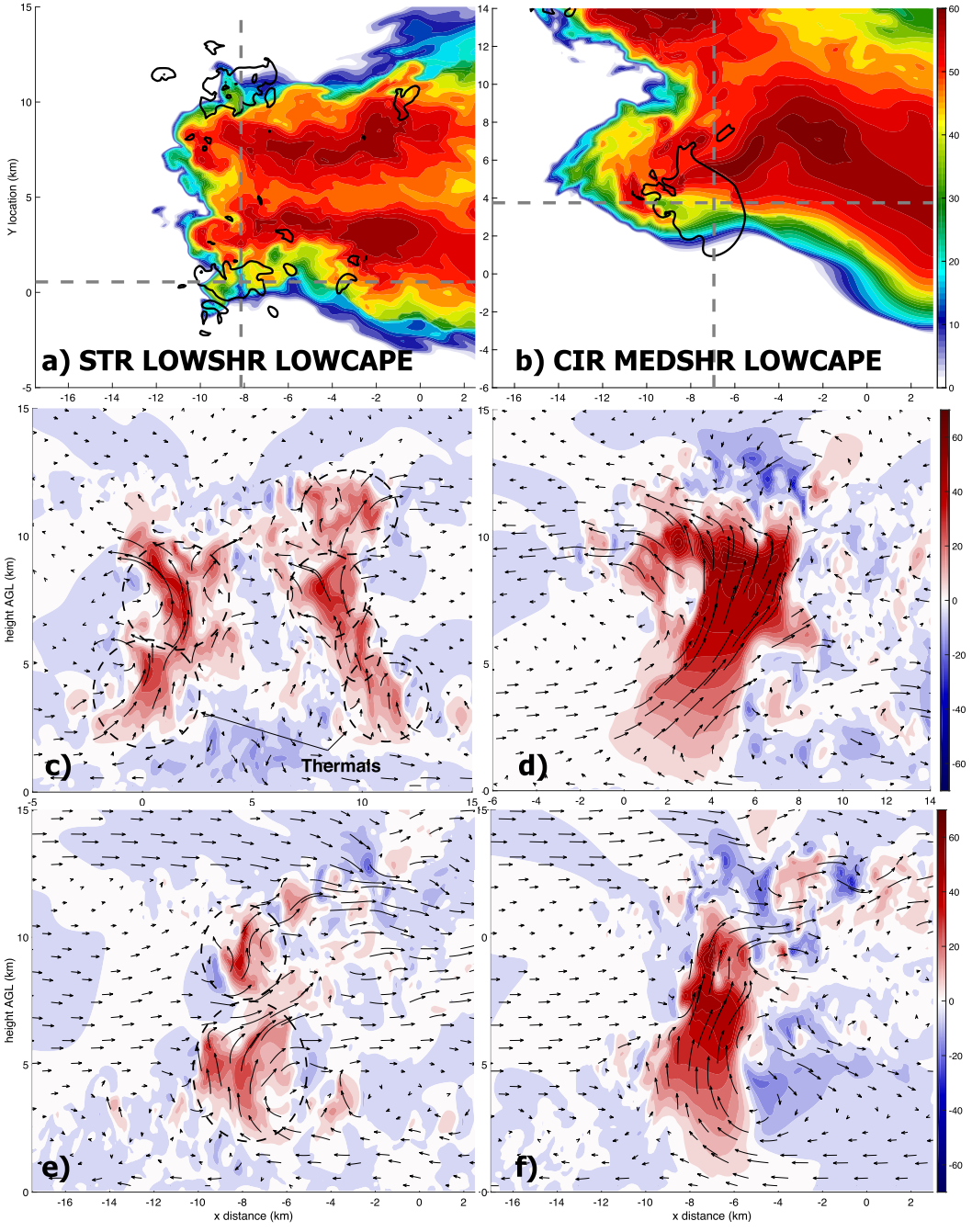

FIG. 5. (a),(b) Plan views of simulated radar reflectivity factor at 1 km (shading; dBZ) and the 6 m s^{-1} 1–4-km mean w contour (solid black line). (c),(d) North-to-south-oriented vertical cross sections along the north-to-south dashed lines in (a) and (b), showing w (shading; m s^{-1}) and streamlines (black curved arrows). (e),(f) As in (c) and (d), but showing east-to-west-oriented vertical cross sections along the east-to-west dashed lines in (a) and (b). (left) The STR LOWSHR LOWCAPE run at 65 min. (right) The CIR MEDSHIR LOWCAPE run at 65 min. The dashed circles in (c) and (e) show the approximate location of individual thermals.

The HISHR experiments unambiguously produced large and persistent classic supercells with steady updrafts, well-defined hook echoes, and expansive V-shaped forward-flank precipitation features (Figs. 3e,f and 4e,f). Vertical cross sections through these storms reveal very large plume-like updrafts with broad continuous regions of strong vertical velocity that extend from just above the ground well into the lower stratosphere (the tropopause

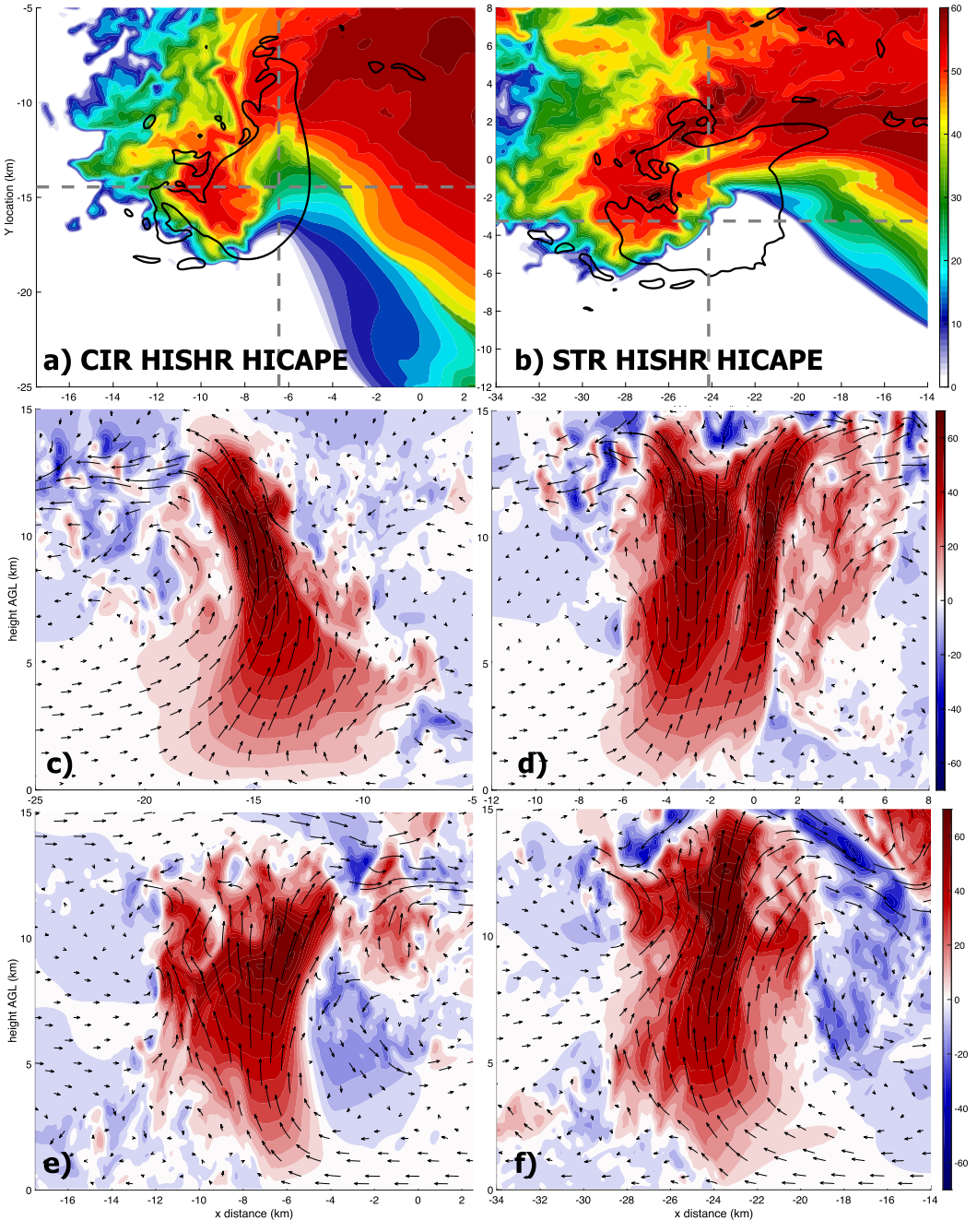

FIG. 6. As in Fig. 5, but for (left) the CIR HISHR HICAPE run at 180 min and (right) the STR HISHR HICAPE run at 180 min.

was set to 12 km in the initial thermodynamic profiles) (Fig. 6). Note that a storm split occurred in the STR simulations; however, because the domain translation speed was designed to center the right-moving storm, the left-moving storm quickly exited the domain. Note also that lateral boundary artifacts are evident along the western flank of several of the HICAPE runs (evident as zonally elongated reflectivity features in Figs. 4c, 4e, and 4f). These artifact features did not approach the primary updraft of interest, and are unlikely to have affected the conclusions of this paper.

b. *Evaluation of hypotheses*

First, we examine the distribution of ϕ within updrafts to determine whether regions of centrifugal stability were present within updrafts. We computed ϕ at each

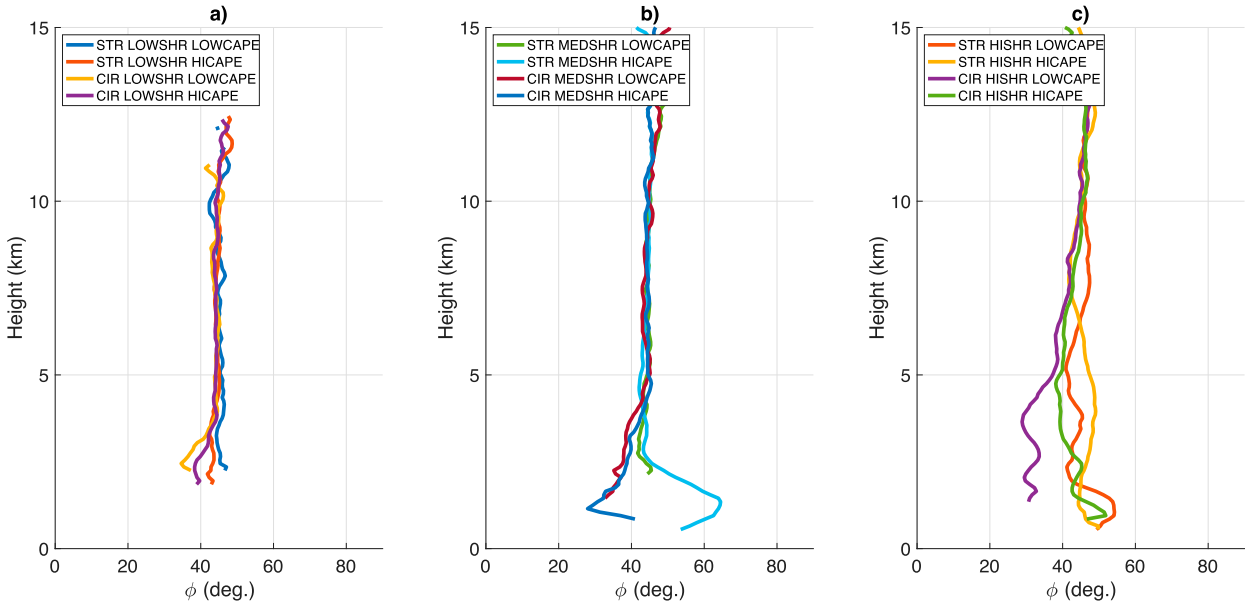

FIG. 7. Vertical profiles of the centrifugal stability parameter ϕ averaged during the 10-min high-temporal-frequency output period. (a) The LOWSHR runs. (b) The MEDSHR runs. (c) The HISHR runs.

grid point, and then horizontally averaged over the extent of the updraft at each height and averaged in time over the period of high-frequency temporal output. Values of ϕ were generally large among all simulations, ranging from 35° to 70° (Fig. 7). Median values of ϕ (not shown) were generally consistent with mean values. Moreover, there is little differentiation in ϕ between supercells and nonsupercells (cf. Figs. 7a,c). This result casts doubt on the centrifugal stability hypothesis, suggesting that expansive regions of balance between the centrifugal force and the pressure gradient force were not present in the updrafts. Visual analysis of the pressure, wind, and w distributions of updrafts at different heights largely affirms this conclusion (e.g., Figs. 8 and 9). Recall that for a centrifugally stable vortex, low pressure must occur at the center of the vortex. In the case of supercell updrafts, if the core were to be protected from lateral mixing via centrifugal stability, we would expect the locally lowest pressure to occur near the updraft center. However, the lowest pressure on a given level within the simulations generally occurred on the eastern and southeastern flanks of the updraft, rather than at the updraft center. This feature was prevalent among both the CIR and STR supercells at all times that we examined and is consistent with negative linear dynamic pressure perturbations on the downshear side of the updraft (e.g., Rotunno and Klemp 1982). Furthermore, there is not clear evidence of 360°, solid-body-like rotation within the flow at any levels (this flow characteristic was also discussed by Dahl 2017). At 3 and 5 km AGL (e.g., Figs. 8a,b and 9a,b), there is evidence of a 180° turn in the flow from westerly on the south flank of the updraft to easterly on the north flank of the updraft, but this circulation is ill-defined on the western flank of the updraft. Above 5 km, there is almost no visual evidence of rotation at all (e.g., Figs. 8c,d and 9c,d).

Next, we determine whether the flow in supercell updrafts is more helical than that of nonsupercells. Values of H_{rel} were horizontally averaged across the updraft, and then averaged in time over the high-temporal-frequency output period. Mean H_{rel} values were very small in the LOWSHR experiments, having maximized at 0.2 near the updraft bases of the CIR simulations and remained generally below 0.1 through most of the updraft depth in both the STR and CIR simulations (Fig. 10a). This definitively indicates that the flow in the nonsupercellular updrafts was *nonhelical* and dominated by crosswise vorticity. Values of H_{rel} were comparatively larger near the base of the CIR MEDSHR updrafts, ranging from 0.25 to 0.75 (Fig. 10b); however, H_{rel} quickly dropped to around 0.1 above 3 km in the CIR simulations, and remained at or below 0.1 in the STR MEDSHR updrafts through most of their depths (Fig. 10b). This indicates that the MEDSHR updrafts were also, for the most part, nonhelical and were dominated by crosswise vorticity above the lowest 3 km of the atmosphere. Values of H_{rel} were the highest in the HISHR experiments, having approached 1 below 3 km in the CIR HICAPE, CIR LOWCAPE, and STR

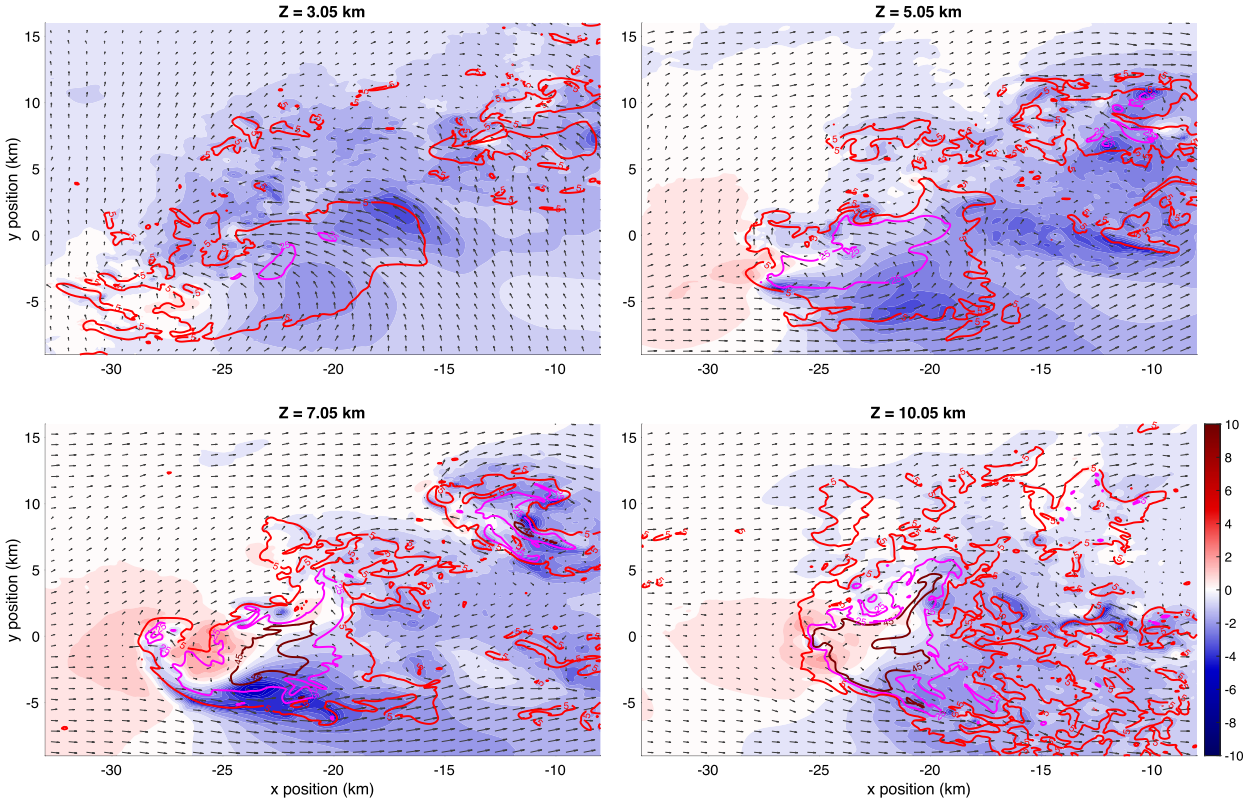

FIG. 8. Plan views of the STR HISHR HICAPE supercell at (a) 3.05, (b) 5.05, (c) 7.05, and (d) 10.05 km, valid at 180 min. Plotted are pressure differences from the initial model profile (shaded; hPa), ground-relative wind vectors (black arrows), and the 5 m s^{-1} (red), 25 m s^{-1} (magenta), and 45 m s^{-1} (dark red) w contours.

HICAPE simulations, and 0.75 in the STR LOWCAPE simulation (Fig. 10c). These values decreased less rapidly with height in the HISHR updrafts than in the LOWSHR and MEDSHR updrafts, remaining near 0.5 in all simulations except STR LOWCAPE at 5 km, and eventually approaching 0.1 by 10 km. Clearly the simulations with the strongest shear that appeared the most supercellular in our qualitative analysis also contained a much higher percentage of streamwise vorticity than the simulations with weaker shear and less pronounced supercell characteristics. Furthermore, both the CIR HISHR simulations had larger H_{rel} than the STR HIRSHR simulations, indicating that larger environmental SRH equates to a larger percentage of streamwise vorticity in the updraft (this trend is also evident when comparing the CIR MEDSHR and STR MEDSHR simulations).

Logarithmic plots of κE computed between 3 and 6 km are examined to determine whether relative helicity in the updraft influences turbulence. The right-hand side of κE curves generally slope downward at approximately $\kappa^{-5/3}$ in all simulations (Figs. 11a–c), indicating well-developed inertial subranges.[2] The $\kappa^{-5/3}$ is especially prevalent in the HISHR supercell experiments, where the approximate $\kappa^{-5/3}$ is maintained all the way from the wavelength of peak energy to the lower resolution bound of the simulation (Fig. 11c). This suggest that, despite the helical nature of flow within supercell updrafts, supercell updrafts—like ordinary convective updrafts—are fully turbulent. This result casts doubt on the helicity hypothesis.

Finally, we examine the entrainment behavior of the simulations as a final assessment of all three hypotheses. The shape of vertical profiles of time-averaged fractional entrainment ε are generally consistent with those of Romps (2010), Fig. 6 therein, with very large ε at low levels within the inflow region of updrafts, and consistently smaller above the inflow regions (Figs. 12a–c).

[2] Note that the apparent "flattening" of the spectra to the right of the energy peaks in the STR MEDSHR LOWCAPE and the CIR MEDSHR LOWCAPE runs (Fig. 11b) is an artifact of the condition that regions of $w < 10$ m s^{-1} were masked out between updrafts, and not indicative of a scale decoupling within these simulations.

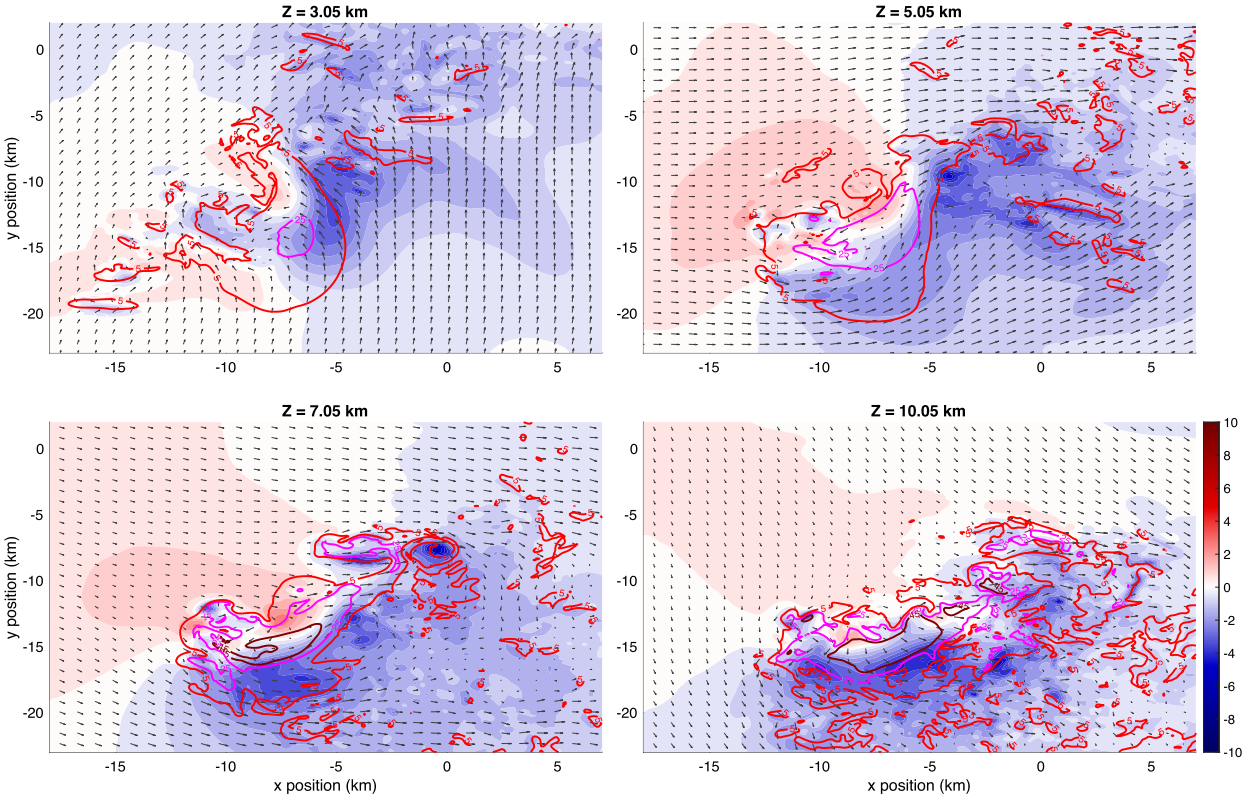

FIG. 9. As in Fig. 8, but for the CIR HISHR HICAPE run at 180 min.

Note that the direct measure of entrainment used here does not discriminate between entrained air with high CAPE that actively participates/drives updraft motions, and entrained air with low or zero CAPE that tends to dilute updraft buoyancy. We must therefore consider the vertical profile of ε in the context of the characteristics of environmental air at each level. For instance, entrained air parcels below 3 km are likely to correspond to large CAPE and will not have a deleterious effect on updraft buoyancy. Conversely, entrained air parcels above 3 km will have no CAPE and will dilute updraft buoyancy. Entrained air parcels above 10 km only affect buoyancy near the tropopause where updraft air has realized most of its CAPE, and consequently have a far lesser effect on updraft buoyancy than those entrained at lower levels. We therefore focus our subsequent analysis of ε to the 3–10-km layer.

Generally, as shear increased, ε decreased (Figs. 12a–c). Recall that our updraft width hypothesis predicts this effect, in that updrafts experiencing shear should be wider and consequently have lower fractional entrainment rates. A comparison of ε with R_{eff}^{-1} shows a very strong correlation between these two variables with $R^2 = 0.95$ and a very small corresponding p value from the Student's t test (Fig. 13a). There is subtle variability in the positioning of simulations relative to the best-fit curves, but no systematic trends to suggest that higher H_{rel} equates to lower entrainment rates independent of the width effect. For instance, CIR runs do not systematically fall to the left of the best-fit line in Fig. 13a (indicating a slight reduction in entrainment for a given R^{-1} due to higher H_{rel}), and STR runs do not systematically fall to the right of the curve (indicating a slight enhancement in entrainment for a given R^{-1} due to lower H_{rel}).

The relationship between ε and 3–10-km H_{rel} (Fig. 13b) is weaker, with $R^2 = 0.57$; furthermore, the presence of fully developed turbulence in all simulated storms suggests that the hypothesized suppressive effects of turbulent entrainment are not at work here. One lingering possibility is that the helical nature of low-level flow in supercells suppresses dynamic entrainment in the low to middle troposphere. This possibility, however, also seems unlikely given that entrainment rates for the STR HISHR updrafts and the CIR HISHR updrafts were relatively similar, despite large differences in H_{rel} among these runs (Fig. 13b). Unsurprisingly, ε and ϕ were not correlated (Fig. 13c). The small ϕ values, combined with the apparent lack of a cyclostrophically balanced vortex in Figs. 8 and 9 further casts doubt on the presence of

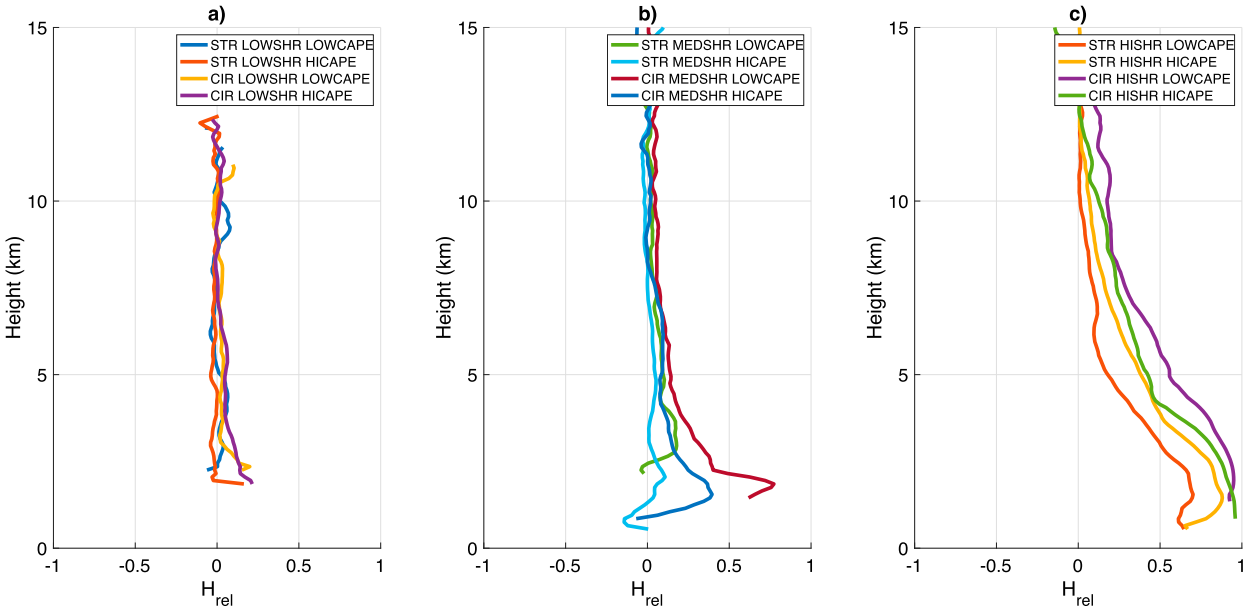

FIG. 10. As in Fig. 7, but for relative helicity.

rotationally driven mechanisms for suppressing dynamic entrainment.

c. *Relationship between entrainment and updraft structure*

The results in the previous section, along with those of our previous work in P19, emphasize that the large widths of supercell updrafts are an important characteristic that substantially reduces the detrimental effects of entrainment on the updraft core, regardless of their rotation. Entrainment process is a powerful regulating factor on the longevity and characteristics of cumulus and cumulonimbus clouds (e.g., Kuang and Bretherton 2006; Khairoutdinov and Randall 2006; Genio and Wu 2010; Romps and Kuang 2010b), and the entrainment of dry middle-tropospheric air can quickly lead to the demise of a developing cloud (as was shown in Morrison 2017). It was further shown by Morrison (e.g., 2017) that the lateral dynamic entrainment of dry air is primarily responsible for the breakdown of updrafts into discrete

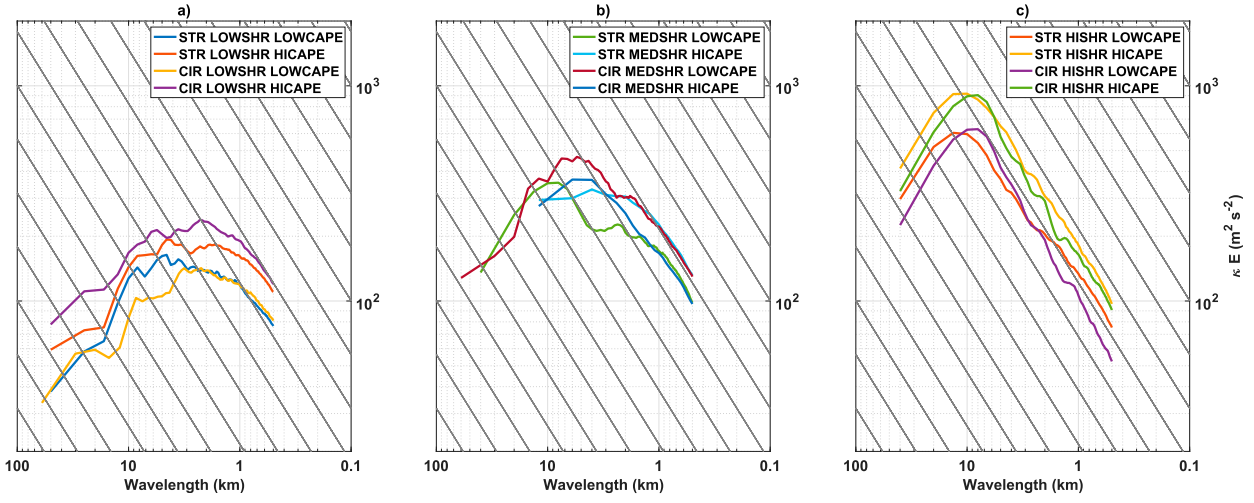

FIG. 11. Fourier energy spectra ($m^2\ s^{-2}$) of w^2 within the updraft region (see text for updraft definitions) computed for each vertical level at each time, and then averaged over the 10-min high-temporal-frequency output period and within the 3–6-km layer. Black lines are the $\kappa^{-5/3}$ curves. (a) The LOWSHR runs. (b) The MEDSHR runs. (c) The HISHR runs. Spectra are truncated at 500 m (5 times the grid spacing), which is the approximate lower bound for proper resolution of processes within the model.

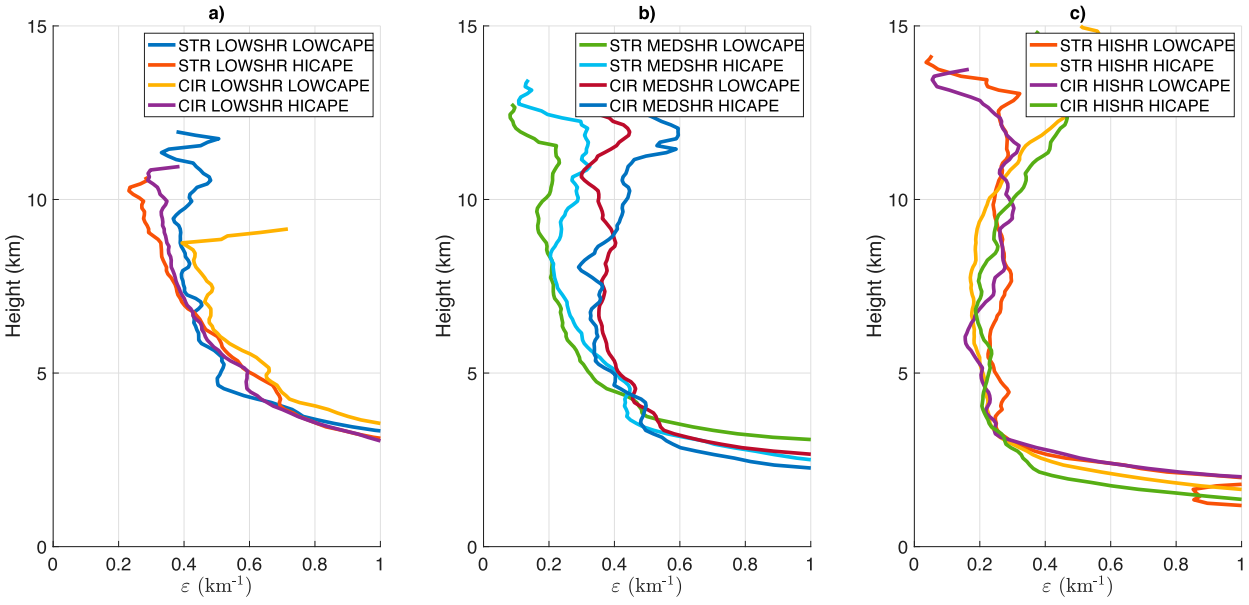

FIG. 12. As in Fig. 7, but for vertical profiles of fractional entrainment ε (km^{-1}).

transient thermals. He found that narrower clouds were most susceptible to this structural breakdown process, having quickly evolved into discrete vertical pulses of updraft that decayed after 10–20 min. In contrast, wider clouds were resistant to this structural breakdown processes, maintaining a continuous plume-like updraft through the depth of the troposphere for an extended period of time. It is therefore possible that the large widths of supercell updrafts relative to ordinary convection, and the associated entrainment reduction, helps to maintain a persistent plume-like structure and to prevent the structural breakdown of supercell updrafts into discrete thermals.

To test the idea that wider updrafts, absent rotation, lead to reductions in entrainment and a more plume-like structure, an additional set of four simulations were performed. These simulations, which used the WK82 sounding with LOWCAPE, were designed to show that even when a constant source of updraft forcing in the boundary layer akin to the low-level dynamic forcing present in supercells, entrainment tends to inhibit the depth, updraft speed, and updraft steadiness of narrow updrafts relative to wider updrafts. These simulations share the modeling configuration of our other simulations with the following exceptions: CM1 V19.8 was used, instead of CM1 V18.0 in the supercell simulations, no initial wind was included to prevent the development of the rotationally driven dynamic pressure forcing features of supercell updrafts, and ice and precipitation microphysics were turned off to exclude the influence of precipitation on updraft evolution [following the experimental methodology of Morrison (2016, 2017) and Morrison and Peters (2018)]. The low-level dynamic forcing present in supercells was emulated using the updraft nudging technique from Naylor and Gilmore (2012) (which is newly included in CM1 V19.8) with updraft nudging centered at 500 m AGL, a vertical radius of forcing of 500 m, a nudging amplitude of 10 m s^{-1}, a nudging e-folding time of 5 s, and nudging widths of 2 km (the FORCE 2-km simulation), 4 km (the FORCE 4-km simulation), 6 km (the FORCE 6-km simulation), and 8 km (the FORCE 8-km simulation) to make the four separate simulations.

Consistent with the results of Morrison (2017), results from the FORCE 2-km simulation show a breakdown of the updraft above the boundary layer into discrete thermals with upward motion largely absent in the vertical spaces between thermals (Fig. 14a), and with updraft top heights intermittently varying between 5 and 8 km (Fig. 15a). As the region of updraft nudging in the boundary layer was expanded in subsequent simulations, the structure of the updraft progressively stabilized and deepened, with stronger updraft in the vertical space between thermals (Fig. 14b) and updraft top heights in the 8–10-km range present in the FORCE 4-km simulation (Fig. 15b) and persistent plume-like structures present in the FORCE 6-km (Fig. 14c) and FORCE 8-km simulations (Fig. 14d) with updraft-top heights above 12 km (Figs. 15c,d). As the boundary layer forcing magnitude was constant among the simulations, the progressive stabilization and deepening of

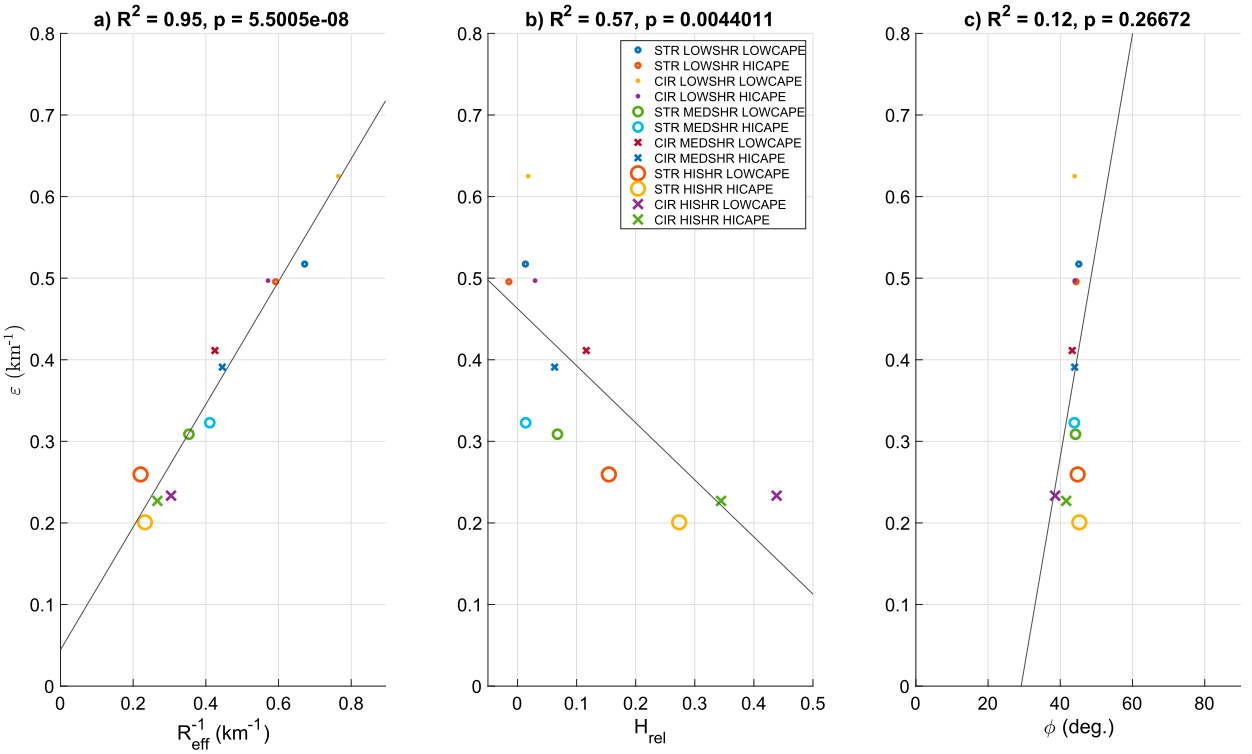

FIG. 13. Comparisons of ε (y axes; km^{-1}) with other updraft properties, with all quantities averaged over the 3–10-km layer. Panels show (a) R_{eff}^{-1}(km^{-1}), (b) H_{rel} (nondimensional), and (c) ϕ (°). Best-fit lines from a linear regression are shown in black, and the coefficient of determination R^2 and the p value based on the Student's t test are shown in the titles of each panel. The × markers represent CIR runs, and ○ markers represent STR runs.

progressively wider updrafts is largely attributable to smaller fractional entrainment rates in the wider updrafts, which reiterates the important influences entrainment has on updraft structure that were discussed by Morrison (2017). Given this evidence, coupled with earlier results that cast doubt on the centrifugal stability and helicity hypotheses, we suggest the possibility that, even with continual low-level updraft forcing, updrafts may not maintain a steady plume-like structure unless they are sufficiently wide. However, we caution the reader that the general applicability of this connection between entrainment, width, and updraft structure is likely to be strongly situationally dependent and requires further investigation.

5. Summary, conclusions, and discussion

This research investigates the role of updraft rotation in modulating entrainment in supercell updrafts. Three hypotheses are investigated: the centrifugal stability hypothesis states that supercell updrafts are centrifugally stable and consequently experience less turbulent entrainment than nonsupercell updrafts; the helicity hypothesis states that the helical nature of flow in supercell updrafts suppresses turbulence and makes supercells less susceptible to the deleterious effects of entrainment on updraft intensity and steadiness than in ordinary nonsupercellular updrafts; finally, the width hypothesis states that supercells are less susceptible to the deleterious effects of entrainment than ordinary nonsupercellular updrafts because of their large widths.

A series of large-eddy simulations was performed to address these hypotheses. The conclusions from our analyses of these simulations are as follows:

- Supercell updrafts (on scales larger than tornadoes) do not appear to resemble centrifugally stable vortices; thus, it is unlikely that centrifugal stability plays a role in mitigating entrainment in supercells.
- A large percentage of the vorticity in the lower part of supercell updrafts is streamwise, in contrast with ordinary updrafts. Despite this distinction, supercell updrafts—like ordinary updrafts—have fully developed turbulence, suggesting that the degree to which updrafts are helical has little influence on turbulent entrainment.
- Fractional entrainment rates tend to be smaller in supercell updrafts than in nonsupercells, but these differences are very strongly correlated with differences in updraft width. Overall, our results support the width hypothesis, and cast doubt on the helical and centrifugal stability hypotheses.

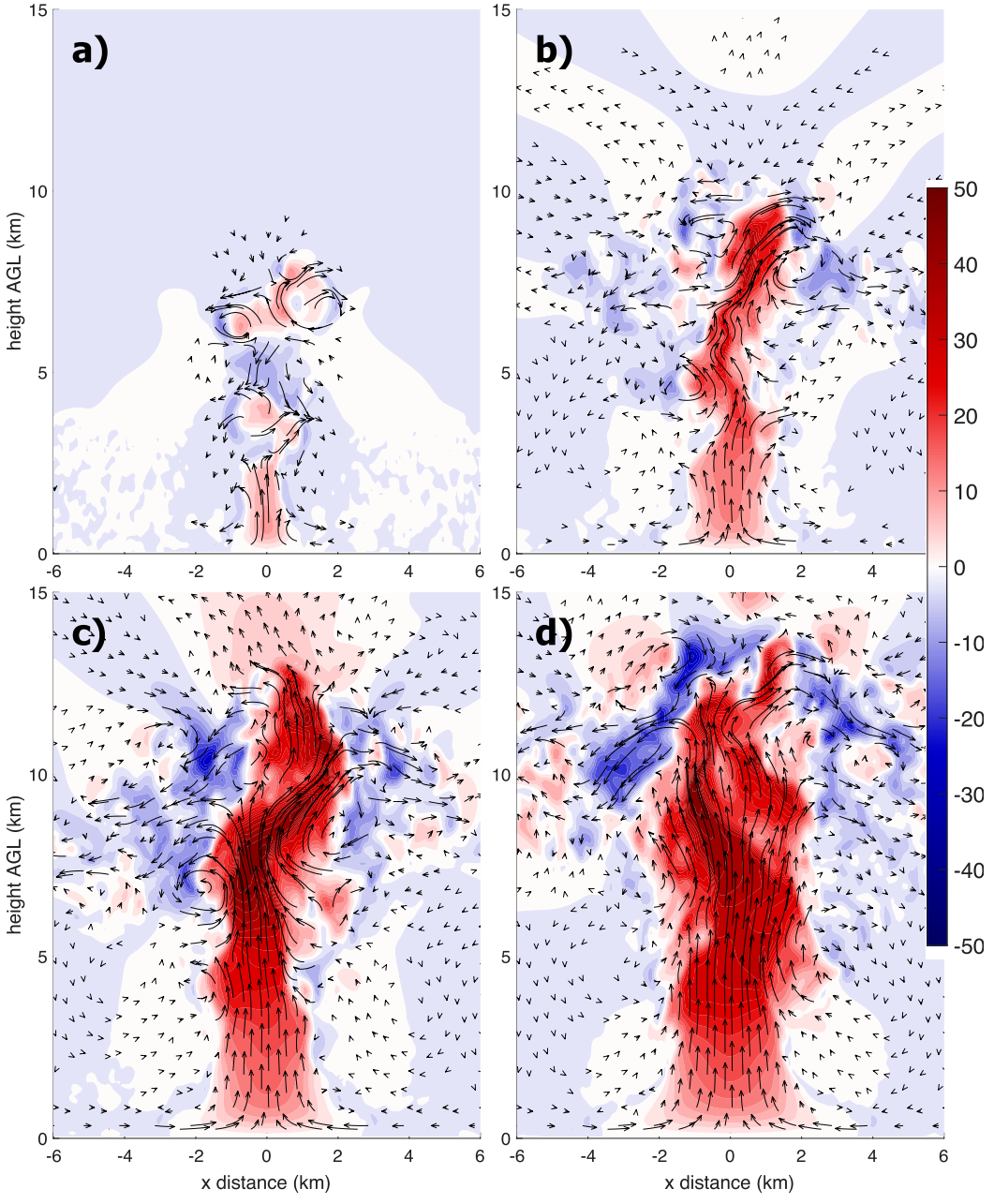

FIG. 14. Vertical cross sections in the x direction through the domain center showing w (shading; m s^{-1}) and streamlines (black arrows) from the (a) FORCE 2-km, (b) FORCE 4-km, (c) FORCE 6-km, and (d) FORCE 8-km runs.

We emphasize that the concrete results in this paper pertain to the connections between updraft rotation, width, and entrainment. A comprehensive assessment of how these properties contribute to updraft persistence is left to future work. We must also reiterate that the discussion here pertains to the role of circulations on the scale of the updraft itself in modulating entrainment. We have not considered tornadoes or pretornadic vortices, nor were any such circulations present during any the periods of the simulations analyzed herein. It is likely that rotationally induced flow stability does influence the entrainment characteristics of tornado-like circulations; however, such circulations are only present during a very small fraction of the life cycles of all supercells, and the rotational and entrainment characteristics of these smaller, more intense vortices therefore cannot explain the overall entrainment resistance of supercell updrafts. Future work

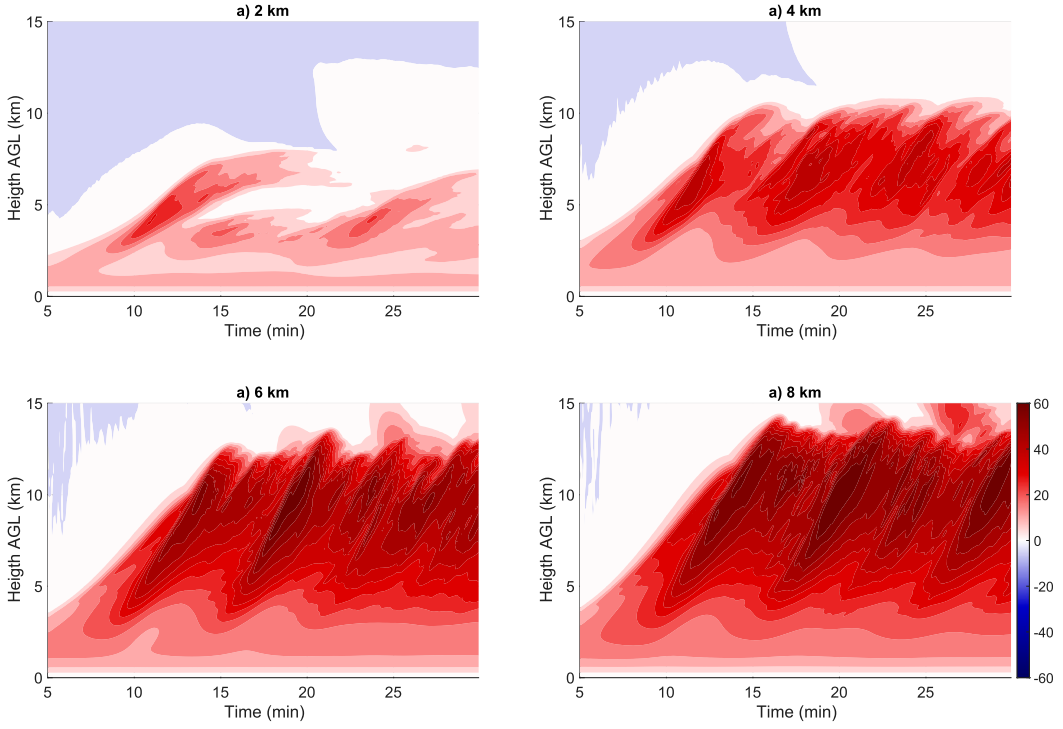

FIG. 15. Time (x axis; min) vs height (y axis; km) diagrams of the horizontal maximum in w (shading, m s^{-1}) from the (a) FORCE 2-km, (b) FORCE 4-km, (c) FORCE 6-km, and (d) FORCE 8-km runs.

should investigate the potential influences of tornadic circulations on the main concepts of this article.

It should also be noted that the simulations here are representative of moderate-to-large-CAPE environments. Important dynamical differences have been found between supercells in moderate-to-large-CAPE environments and those in environments with weak CAPE but strong shear (e.g., McCaul and Weisman 1996). A reinvestigation of the hypotheses addressed here in environments with weaker CAPE and stronger shear is therefore warranted.

Acknowledgments. J. Peters's and C. Nowotarski's efforts were supported by the National Science Foundation (NSF) Grants AGS-1928666 and AGS-1928319, respectively. Additionally, J. Peters was partially supported by NSF Grant AGS-1841674 and Department of Energy Atmospheric System Research Grant DE-SC0000246356. Finally, we are grateful for the helpful comments from three anonymous peer reviewers.

REFERENCES

André, J. C., and M. Lesieur, 1977: Influence of helicity on the evolution of isotropic turbulence at high Reynolds number. *J. Fluid Mech.*, **81**, 187–207, https://doi.org/10.1017/S0022112077001979.

Brandes, E. A., R. P. Davies-Jones, and B. C. Johnson, 1988: Streamwise vorticity effects on supercell morphology and persistence. *J. Atmos. Sci.*, **45**, 947–963, https://doi.org/10.1175/1520-0469(1988)045<0947:SVEOSM>2.0.CO;2.

Bryan, G. H., and J. M. Fritsch, 2002: A benchmark simulation for moist nonhydrostatic numerical models. *Mon. Wea. Rev.*, **130**, 2917–2928, https://doi.org/10.1175/1520-0493(2002)130<2917:ABSFMN>2.0.CO;2.

——, J. C. Wyngaard, and J. M. Fritsch, 2003: Resolution requirements for the simulation of deep moist updrafts. *Mon. Wea. Rev.*, **131**, 2394–2416, https://doi.org/10.1175/1520-0493(2003)131<2394:RRFTSO>2.0.CO;2.

Bunkers, M. J., B. A. Klimowski, R. L. Thompson, and M. L. Weisman, 2000: Predicting supercell motion using a new hodograph technique. *Wea. Forecasting*, **15**, 61–79, https://doi.org/10.1175/1520-0434(2000)015<0061:PSMUAN>2.0.CO;2.

Dahl, J. M. L., 2017: Tilting of horizontal shear vorticity and the development of updraft rotation in supercell thunderstorms. *J. Atmos. Sci.*, **74**, 2997–3020, https://doi.org/10.1175/JAS-D-17-0091.1.

Davies-Jones, R. P., R. J. Trapp, and H. B. Bluestein, 2001: Tornadoes and tornadic storms. *Severe Convective Storms*, *Meteor. Monogr.*, No. 50, Amer. Meteor. Soc., 167–222.

Dawe, J. T., and P. H. Austin, 2011: Interpolation of LES cloud surfaces for use in direct calculations of entrainment and detrainment. *Mon. Wea. Rev.*, **139**, 444–456, https://doi.org/10.1175/2010MWR3473.1.

De Rooy, W. C., and A. P. Siebesma, 2010: Analytical expressions for entrainment and detrainment in cumulus convection. *Quart. J. Roy. Meteor. Soc.*, **136**, 1216–1227, https://doi.org/10.1002/QJ.640.

DiGangi, E. A., D. R. MacGorman, C. L. Ziegler, D. Betten, M. Biggerstaff, M. Bowlan, and C. K. Potvin, 2016: An overview of the 29 May 2012 Kingfisher supercell during DC3. *J. Geophys. Res. Atmos.*, **121**, 14 316–14 343, https://doi.org/10.1002/2016JD025690.

Doswell, C. A., and D. Burgess, 1993: Tornadoes and tornadic storms: A review of conceptual models. *The Tornado: Its Structure, Dynamics, Prediction, and Hazards*, *Geophys. Monogr.*, Vol. 79, Amer. Geophys. Union, 161–172.

Durran, D. R., and J. B. Klemp, 1983: A compressible model for the simulation of moist mountain waves. *Mon. Wea. Rev.*, **111**, 2341–2361, https://doi.org/10.1175/1520-0493(1983)111<2341:ACMFTS>2.0.CO;2.

Genio, A. D. D., and J. Wu, 2010: The role of entrainment in the diurnal cycle of continental convection. *J. Climate*, **23**, 2722–2738, https://doi.org/10.1175/2009JCLI3340.1.

Hernandez-Deckers, D., and S. C. Sherwood, 2016: A numerical investigation of cumulus thermals. *J. Atmos. Sci.*, **73**, 4117–4136, https://doi.org/10.1175/JAS-D-15-0385.1.

Holton, J. R., 2004: *An Introduction to Dynamic Meteorology*. Academic Press, 535 pp.

Khairoutdinov, M., and D. A. Randall, 2006: High-resolution simulation of shallow-to-deep convective transition over land. *J. Atmos. Sci.*, **63**, 3421–3436, https://doi.org/10.1175/JAS3810.1.

Klemp, J. B., R. B. Wilhelmson, and P. S. Ray, 1981: Observed and numerically simulated structure of a mature supercell thunderstorm. *J. Atmos. Sci.*, **38**, 1558–1580, https://doi.org/10.1175/1520-0469(1981)038<1558:OANSSO>2.0.CO;2.

Kuang, Z., and C. S. Bretherton, 2006: A mass flux scheme view of a high-resolution simulation of a transition from shallow to deep cumulus convection. *J. Atmos. Sci.*, **63**, 1895–1909, https://doi.org/10.1175/JAS3723.1.

Lebo, Z. J., and H. Morrison, 2015: Effects of horizontal and vertical grid spacing on mixing in simulated squall lines and implications for convective strength and structure. *Mon. Wea. Rev.*, **143**, 4355–4375, https://doi.org/10.1175/MWR-D-15-0154.1.

Lecoanet, D., and N. Jeevanjee, 2019: Entrainment in resolved, dry thermals. *J. Atmos. Sci.*, **76**, 3785–3801, https://doi.org/10.1175/JAS-D-18-0320.1.

Lehmiller, G. S., H. B. Bluestein, P. J. Neiman, F. M. Ralph, and W. F. Feltz, 2001: Wind structure in a supercell thunderstorm as measured by a UHF wind profiler. *Mon. Wea. Rev.*, **129**, 1968–1986, https://doi.org/10.1175/1520-0493(2001)129<1968:WSIAST>2.0.CO;2.

Lilly, D. K., 1986: The structure, energetics, and propagation of rotating convective storms. Part II: Helicity and storm stabilization. *J. Atmos. Sci.*, **43**, 126–140, https://doi.org/10.1175/1520-0469(1986)043<0126:TSEAPO>2.0.CO;2.

Markowski, P., and Y. Richardson, 2010: *Mesoscale Meteorology in Midlatitudes*. Wiley-Blackwell, 430 pp.

McCaul, E. W., and M. L. Weisman, 1996: Simulations of shallow supercell storms in landfalling hurricane environments. *Mon. Wea. Rev.*, **124**, 408–429, https://doi.org/10.1175/1520-0493(1996)124<0408:SOSSSI>2.0.CO;2.

Morrison, H., 2016: Impacts of updraft size and dimensionality on the perturbation pressure and vertical velocity in cumulus convection. Part II: Comparison of theoretical and numerical solutions and fully dynamical simulations. *J. Atmos. Sci.*, **73**, 1455–1480, https://doi.org/10.1175/JAS-D-15-0041.1.

——, 2017: An analytic description of the structure and evolution of growing deep cumulus updrafts. *J. Atmos. Sci.*, **74**, 809–834, https://doi.org/10.1175/JAS-D-16-0234.1.

——, and J. M. Peters, 2018: Theoretical expressions for the ascent rate of moist convective thermals. *J. Atmos. Sci.*, **75**, 1699–1719, https://doi.org/10.1175/JAS-D-17-0295.1.

——, G. Thompson, and V. Tatarskii, 2009: Impact of cloud microphysics on the development of trailing stratiform precipitation in a simulated squall line: Comparison of one- and two-moment schemes. *Mon. Wea. Rev.*, **137**, 991–1007, https://doi.org/10.1175/2008MWR2556.1.

Naylor, J., and M. S. Gilmore, 2012: Convective initiation in an idealized cloud model using an updraft nudging technique. *Mon. Wea. Rev.*, **140**, 3699–3705, https://doi.org/10.1175/MWR-D-12-00163.1.

Peters, J. M., W. M. Hannah, and H. Morrison, 2019a: The influence of vertical wind shear on moist thermals. *J. Atmos. Sci.*, **76**, 1645–1659, https://doi.org/10.1175/JAS-D-18-0296.1.

——, C. Nowotarski, and H. Morrison, 2019b: The role of vertical wind shear in modulating maximum supercell updraft velocities. *J. Atmos. Sci.*, **76**, 3169–3189, https://doi.org/10.1175/JAS-D-19-0096.1.

Peterson, D. A., J. R. Campbell, E. J. Hyer, M. D. Fromm, G. P. Kablick, J. H. Cossuth, and M. T. Deland, 2018: Wildfire-driven thunderstorms cause a volcano-like stratospheric injection of smoke. *npj Climate Atmos. Sci.*, **1**, 30, https://doi.org/10.1038/S41612-018-0039-3.

Potvin, C. K., and M. L. Flora, 2015: Sensitivity of idealized supercell simulations to horizontal grid spacing: Implications for Warn-on-Forecast. *Mon. Wea. Rev.*, **143**, 2998–3024, https://doi.org/10.1175/MWR-D-14-00416.1.

Romps, D. M., 2010: A direct measure of entrainment. *J. Atmos. Sci.*, **67**, 1908–1927, https://doi.org/10.1175/2010JAS3371.1.

——, and Z. Kuang, 2010a: Do undiluted convective plumes exist in the upper troposphere? *J. Atmos. Sci.*, **67**, 468–484, https://doi.org/10.1175/2009JAS3184.1.

——, and ——, 2010b: Nature versus nurture in shallow convection. *J. Atmos. Sci.*, **67**, 1655–1666, https://doi.org/10.1175/2009JAS3307.1.

——, and A. B. Charn, 2015: Sticky thermals: Evidence for a dominant balance between buoyancy and drag in cloud updrafts. *J. Atmos. Sci.*, **72**, 2890–2901, https://doi.org/10.1175/JAS-D-15-0042.1.

Rotunno, R., and J. B. Klemp, 1982: The influence of the shear-induced pressure gradient on thunderstorm motion. *Mon. Wea. Rev.*, **110**, 136–151, https://doi.org/10.1175/1520-0493(1982)110<0136:TIOTSI>2.0.CO;2.

——, and ——, 1985: On the rotation and propagation of simulated supercell thunderstorms. *J. Atmos. Sci.*, **42**, 271–292, https://doi.org/10.1175/1520-0469(1985)042<0271:OTRAPO>2.0.CO;2.

Sherwood, S. C., D. Hernandez-Deckers, and M. Colin, 2013: Slippery thermals and the cumulus entrainment paradox. *J. Atmos. Sci.*, **70**, 2426–2442, https://doi.org/10.1175/JAS-D-12-0220.1.

Tarshish, N., N. Jeevanjee, and D. Lecoanet, 2018: Buoyant motion of a turbulent thermal. *J. Atmos. Sci.*, **75**, 3233–3244, https://doi.org/10.1175/JAS-D-17-0371.1.

Trapp, R. J., G. R. Marion, and S. W. Nesbitt, 2017: The regulation of tornado intensity by updraft width. *J. Atmos. Sci.*, **74**, 4199–4211, https://doi.org/10.1175/JAS-D-16-0331.1.

Warren, R. A., H. Richter, H. A. Ramsay, S. T. Siems, and M. J. Manton, 2017: Impact of variations in upper-level shear on simulated supercells. *Mon. Wea. Rev.*, **145**, 2659–2681, https://doi.org/10.1175/MWR-D-16-0412.1.

Weisman, M. L., and J. B. Klemp, 1982: The dependence of numerically simulated convective storms on vertical wind shear and buoyancy. *Mon. Wea. Rev.*, **110**, 504–520, https://doi.org/10.1175/1520-0493(1982)110<0504:TDONSC>2.0.CO;2.

——, and ——, 1984: The structure and classification of numerically simulated convective storms in directionally varying wind shears. *Mon. Wea. Rev.*, **112**, 2479–2498, https://doi.org/10.1175/1520-0493(1984)112<2479:TSACON>2.0.CO;2.

——, and R. Rotunno, 2000: The use of vertical wind shear versus helicity in interpreting supercell dynamics. *J. Atmos. Sci.*, **57**, 1452–1472, https://doi.org/10.1175/1520-0469(2000)057<1452:TUOVWS>2.0.CO;2.